

eISSN (Online): 2598-0580

Bioscientia Medicina: Journal of Biomedicine & Translational Research

Journal Homepage: www.bioscmed.com

Personalized Periodontal Regeneration: Integrating 3D Bioprinting with Autologous Activated Growth Factor (AGF) for Enhanced Alveolar Bone Defect Healing via an In Silico, In Vitro, and In Vivo Approach

Zelka Dapala[1], Rachmat Hidayat[2*], Muhammad Ashraf[3]

[1]Department of Dentistry, Faculty of Medicine, Universitas Sriwijaya, Palembang, Indonesia
[2]Department of Medical Biology, Faculty of Medicine, Universitas Sriwijaya, Palembang, Indonesia
[3]Department of Oral Health and Dentistry, Phlox Institute, Palembang, Indonesia

ARTICLE INFO

Keywords:
alveolar bone loss
bioprinting
guided periodontal tissue regeneration
hydrogels
intercellular signaling peptides and proteins

***Corresponding author:**
Rachmat Hidayat
E-mail address:
dr.rachmat.hidayat@gmail.com
ORCID: 0000-0001-5770-1201

All authors have reviewed and approved the final version of the manuscript.
https://doi.org/10.37275/bsm.v9i12.1605

A B S T R A C T

Background: Conventional grafting of Stage III–IV infrabony defects often heals by long junctional epithelium. Causes include geometric mismatch. Soluble biologics also wash out rapidly. **Objective:** To evaluate a patient-specific, biphasic 3D-bioprinted gelatin methacryloyl–heparin methacryloyl/nanohydroxyapatite (GelMA–HepMA/nHAp) scaffold bio-integrated with autologous activated growth factor (AGF). **Methods:** Phase I used finite element, computational fluid dynamics, and docking simulations. Phase II (N = 24) comprised 4-arm rheology, 21-day ELISA release, human periodontal ligament stem cell (hPDLSC), and endothelial assays. Phase III (N = 40) used critical-size (5.0 × 3.0 × 2.0 mm) rat mandibular defects, assessed at Weeks 4 and 8 by micro-CT, histomorphometry, and immunohistochemistry. **Results:** The triply periodic minimal surface Schoen Gyroid lattice was favored in simulation (effective modulus 149.16 MPa; 91.6% of surface in the osteogenic wall shear stress window). Docking predicted nanomolar sulfated HepMA affinity for PDGF-BB, VEGF-A165, and TGF-β1 (−10.32 to −10.96 kcal/mol). PDGF-BB burst release at 24 hours fell from 79.4 ± 4.2% to 19.8 ± 2.1% ($p < 0.001$). The 3DBP–HepMA–AGF construct gave the highest hPDLSC mineralization and RUNX2, SP7, CEMP1, and POSTN expression in vitro. At Week 8, it gave the highest bone volume fraction (76.4 ± 3.9% vs. 22.4 ± 2.8% in controls; $p < 0.001$), neocementum thickness (64.2 ± 4.8 μm), and Sharpey's fiber angle (50.8 ± 3.2°). **Conclusion:** In this rat model, CBCT-guided biphasic affinity bioprinting with autologous AGF was associated with sustained release in vitro. It also gave the greatest bone, cementum, and oriented fiber formation in vivo. Larger studies are needed.

1. Introduction

Severe periodontitis is a major global public health burden that affects more than one billion adults worldwide. It is a principal cause of premature tooth loss, masticatory dysfunction, oral-systemic low-grade inflammation, and reduced quality of life through mid-century demographic projections.[1,2] Severe periodontitis burden has also been quantified among women of childbearing age.[3] Under the consensus framework of the World Workshop on the Classification of Periodontal and Peri-Implant Diseases and Conditions, Stage III and Stage IV periodontitis are defined by deep vertical infrabony defects, furcation involvement, secondary occlusal trauma, and progressive loss of the attachment apparatus supporting the dentition.[4] Current European Federation of Periodontology (EFP) S3-level clinical practice guidelines endorse regenerative surgery. The guidelines apply to residual intrabony defects measuring three millimeters or deeper. They list barrier membranes for guided tissue regeneration (GTR), enamel matrix derivatives, and particulate autogenous, allogeneic, or xenogeneic bone grafts as options.[5,6] Predictability declines sharply in non-contained one-wall, wide two-wall, and complex crateriform alveolar architectures. There, mucoperiosteal flap compression, graft particle

micromotion, and microbial contamination routinely divert wound healing toward reparative long junctional epithelial downgrowth or parallel collagenous encapsulation, and genuine anatomical restitution does not occur.[6,7]

True periodontal regeneration demands the spatiotemporal re-assembly of a load-bearing tri-phasic organ. It comprises vascularized alveolar bone proper, acellular and cellular extrinsic fiber cementum deposited along the denuded root dentin, and an interposed, unmineralized periodontal ligament (PDL) that spans 150 to 250 micrometers in width and is anchored by obliquely oriented (45° to 60°) Sharpey's collagen fiber bundles.[7–9] Conventional particulate bone substitutes act mainly as osteoconductive space fillers. They lack patient-specific macro-geometric conformity. They also cannot establish the micrometer-scale compartmentalization needed to separate osteogenesis from the root surface, so osteoprogenitor cells colonize the denuded cementum unchecked, and dentoalveolar ankylosis and replacement root resorption ensue.[9–11] Over the past five years, digital workflows have emerged that link high-resolution cone-beam computed tomography (CBCT) segmentation with computer-aided design (CAD) and extrusion-based three-dimensional (3D) bioprinting.[8,10–14] These workflows fabricate constructs matched to irregular infrabony morphologies. Multiphasic bioprinted scaffolds co-deposit mineralized osteogenic hydrogels with softer, topographically micro-channeled periodontal interface layers. This design can eliminate dead space at the defect margins and stabilize the blood clot below the threshold of deleterious occlusal micromotion. It also gives contact guidance cues that orient migrating periodontal progenitor cells toward the root surface.[8,15,16]

Additive manufacturing has advanced greatly. Even so, two biophysical and pharmacological barriers still impede clinical translation of personalized periodontal constructs. First, most first-generation printed bone scaffolds rely on rectilinear 0°/90° orthogonal filament grids, which produce sharp right-angle stress concentrations under oblique masticatory loading and create stagnant microfluidic zones that impair nutrient transport and core neovascularization.[17–19] Sheet- and network-based triply periodic minimal surface (TPMS) architectures offer an alternative. The best known is the Schoen Gyroid topology. Its features are zero mean surface curvature, interconnected tortuous pore networks, near-isotropic load transfer, and elevated Darcy permeability, which can translate physiological interstitial fluid flow into uniform mechanotransductive wall shear stress across internal pore walls.[17–21] Second, structural polymeric-ceramic frameworks composed of gelatin methacryloyl (GelMA) and nanohydroxyapatite (nHAp) are predominantly osteoconductive and mechanically tunable.[22–27] They lack, however, the endogenous temporal cascade of chemotactic, mitogenic, angiogenic, and cementogenic morphogens needed to recruit host stem cells into large avascular osseous defects.[12–14,28]

Single recombinant human proteins carry prohibitive cost, supraphysiological risks of ectopic ossification, and immunogenicity. Autologous platelet-derived biologics avoid these drawbacks while supplying bioactive instructive cues, and they have attracted intense translational interest in reconstructive periodontology.[7,29–35] Examples are platelet-rich plasma (PRP), platelet-rich fibrin (PRF), and cell-free Autologous Activated Growth Factor (AGF) concentrates. AGF is prepared by differential centrifugation and controlled calcium-thrombin degranulation of autologous platelets, and it delivers a physiological cocktail of platelet-derived growth factor-BB (PDGF-BB), vascular endothelial growth factor-A165 (VEGF-A165), transforming growth factor-β1 (TGF-β1), and insulin-like growth factor-1 (IGF-1) that mimics the native wound-healing secretome.[7,31,32] When AGF is applied as uncrosslinked fibrin gels or passively imbibed into unmodified hydrogels, soluble cytokines undergo rapid burst washout exceeding 70% to 80% within the first 24 hours (as observed here for passive loading; 72.6%–79.4%), and enzymatic

proteolysis within gingival crevicular fluid degrades them quickly. Biological signaling therefore ends well before osteoblastic mineralization and cementogenesis peak between days 14 and 21.[28,32,36–38] Functionalizing the GelMA hydrogel network with covalently crosslinkable sulfated heparin methacryloyl (HepMA) offers a biomimetic solution. By emulating extracellular matrix heparan sulfate proteoglycans, immobilized sulfate groups engage basic arginine- and lysine-rich heparin-binding domains (HBDs) on PDGF-BB, VEGF-A165, and TGF-β1 through reversible non-covalent salt bridges. Labile growth factors are thus shielded from proteolysis, and their release is sustained.[28,36–39]

Three questions remain open; the first two are addressed by simulation and the third by experiment. First, does an implicit TPMS Schoen Gyroid topology outperform conventional rectilinear lattices in balancing occlusal load sharing with osteoinductive microfluidic shear? Second, does covalent sulfated HepMA functionalization sequester autologous AGF morphogens without distorting their receptor-binding epitopes? Third, do bio-integrated 3DBP–AGF constructs generate effects in vivo greater than either 3D-bioprinted scaffolds alone or autologous AGF gels alone? Accordingly, the present Original Research Article carried out a sequential tri-modal in silico, in vitro, and in vivo translational investigation to engineer, optimize, and evaluate a CBCT-matched, biphasic GelMA–HepMA/nHAp construct bio-integrated with leukocyte-modulated autologous AGF for alveolar bone, cementum, and periodontal ligament regeneration.

2. Methods

Study design and ethical approval

The study followed a three-phase translational pipeline. Phase I was computational optimization, covering in silico finite element analysis, computational fluid dynamics perfusion modeling, molecular docking, and coupled reaction-diffusion-binding partial differential equation simulation. Phase II was biomaterial-cellular validation. It comprised 4-arm factorial in vitro rheological characterization, CAD-to-print geometric metrology, 21-day cytokine release kinetics, and hPDLSC/endothelial co-functional bioassays (N = 24 independent constructs, n = 6 per group). Phase III was preclinical surgical verification. It was a randomized, controlled, assessor-blinded in vivo evaluation in critical-size mandibular buccal alveolar–PDL fenestration defects in adult male Wistar rats, with N = 40 animals across four surgical arms and two postoperative endpoints at Week 4 and Week 8 (n = 5 rats per group per timepoint). All animal surgical and husbandry procedures were designed and executed in strict accordance with the updated ARRIVE 2.0 guidelines for reporting animal research,[40] national regulations on laboratory animal welfare, and institutional ethical clearance. The Ethics Committee of CMHC Research Center approved the protocol (Protocol Number: 331/2025).

Phase I: CBCT-to-CAD modeling, finite element analysis, and perfusion simulation

A representative three-wall mandibular molar infrabony and buccal fenestration defect geometry was segmented from anonymized high-resolution CBCT DICOM volumes (isotropic voxel size 80 μm). Thresholding and Boolean subtraction generated watertight stereolithography (STL) meshes.[10,11] The construct was partitioned into two monolithic, continuous compartments. The outer one was a load-sharing alveolar osteogenic zone. The inner one was a 460-μm-thick root-facing PDL-guiding interface designed with parallel 150-μm-wide apicocoronal micro-grooves separated by 25-μm guidance ridges (CAD design dimensions; printed fidelity is reported as CAD-to-print RMSD), which was intended to direct oblique collagen fiber insertion.[8,15] Within the osteogenic compartment, three candidate open-cell unit-cell topologies were parametrically generated at matched target macroporosity ($\varphi \approx 68.0\%$) and mean interconnected pore diameter (415–420 μm): an Orthogonal 0°/90° rectilinear Grid (OG), a Honeycomb Hexagonal lattice (HH), and an implicit Triply Periodic Minimal Surface Schoen Gyroid (SG). The gyroid followed the level-set equation $\sin(2\pi x/L)\cos(2\pi y/L) +$

$\sin(2\pi y/L)\cos(2\pi z/L) + \sin(2\pi z/L)\cos(2\pi x/L) = t_0$. The unit-cell periodicity was L = 0.85 mm.[17–20] Three-dimensional tetrahedral finite element meshes (~4.2 × 10^5 quadratic elements after mesh-convergence verification within <1.5% peak stress change) were solved under a physiological oblique masticatory load of 150 N inclined at 30° to the long axis of the mandibular molar.

The solutions gave the effective compressive modulus (E* via Gibson–Ashby homogenization), peak Von Mises stress ($\sigma_{VM,max}$), stress-concentration factor (K_t), structural yield safety factor (SF), and root-scaffold interfacial micromotion (μm).[17,19] The simulated E* describes the modeled lattice, whereas the Phase II moduli were measured on hydrated hydrogel constructs, so the two are not directly comparable. Incompressible laminar Navier–Stokes computational fluid dynamics (CFD) simulations used an interstitial inlet velocity of 0.10 mm/s, a perfusate dynamic viscosity of $\mu = 1.0 \times 10^{-3}$ Pa·s, and a density of ρ = 1,005 kg/m³. They returned intrinsic Kozeny–Carman Darcy permeability (k) and surface wall shear stress (τ_w). The mechanobiologically osteogenic surface fraction was defined within $\tau_w \in [1.0, 10.0]$ mPa.[17,18]

Phase I: heparin-affinity docking and reaction-diffusion-binding simulation

Atomic coordinates of four principal osteo-angiogenic cytokines were retrieved from the RCSB Protein Data Bank. These cytokines are enriched in activated platelet secretomes or recruited endogenously: human PDGF-BB homodimer (PDB ID: 3MJG), VEGF-A165 heparin-binding domain (PDB ID: 3V2A), active TGF-β1 homodimer (PDB ID: 3KFD), and BMP-2 homodimer (PDB ID: 1REW). Each structure was protonated at physiological pH 7.4 and energy-minimized under the AMBER ff14SB force field.

Representative pentameric hydrogel oligomer motifs for unmodified methacrylated gelatin (GelMA) and for O-/N-sulfated heparin methacryloyl–conjugated GelMA (GelMA–HepMA, carrying $-SO_3^-$ and $-COO^-$ anionic groups) were geometry-optimized using semi-empirical PM7/MMFF94s charges. Flexible-ligand molecular docking with Molecular Mechanics Generalized Born Surface Area (MM-GBSA) rescoring at T = 310.15 K evaluated binding free energies (ΔG_{bind}, kcal/mol), equilibrium dissociation constants ($K_d = \exp(\Delta G_{bind}/RT)$), intermolecular hydrogen bonds, Arg/Lys–sulfate salt bridges, and root-mean-square deviation (RMSD) of receptor-binding epitopes. This ensured preservation of downstream receptor bioactivity.[28,36,37] The derived K_d values parameterized a coupled reversible reaction-diffusion-erosion partial differential equation system. Fifth-order Runge–Kutta integration (RK45, relative tolerance 10^{-7}) solved it numerically over 504 hours (21 days). The simulation compared passive Fickian diffusion from unmodified GelMA/nHAp with electrostatic sequestration in GelMA–HepMA/nHAp.[28,36]

Autologous activated growth factor preparation and quality control

Blood was collected into sterile acid-citrate-dextrose formula A (ACD-A, 1:9 v/v) tubes. Whole venous blood totaled 10 mL per donor batch in vitro, whereas in vivo collection used 1.8 mL by autologous tail/jugular venipuncture with physiological saline given to replace the volume drawn, and all samples underwent standardized two-step differential centrifugation at 22°C.[31,32] The initial soft spin ran at 300 × g for 10 minutes. It separated erythrocytes from the plasma-platelet supernatant. A concentration spin at 1,200 × g for 15 minutes followed, during which the leukocyte-poor platelet pellet zone and buffy-coat boundary were aspirated selectively so that carryover of neutrophil elastase and pro-inflammatory metalloproteinases stayed limited.[29,32]

Platelet counts were verified hematologically. Activation then used sterile 10% calcium chloride (final Ca^{2+} concentration 22.8 mM) combined with autologous thrombin-rich serum (1:5 v/v) at 37°C for 30 minutes, after which the material was centrifuged at 3,000 × g for 10 minutes and passed through low-protein-binding 0.22-μm polyethersulfone membranes by sterile filtration to yield a cell-free, standardized AGF concentrate.[7,32] Baseline concentrations of

PDGF-BB, VEGF-A165, TGF-β1, and IGF-1 were quantified across six independent batches by sandwich enzyme-linked immunosorbent assay (ELISA) before bioink incorporation. Together with sterile 0.22-μm filtration, this leukocyte-poor aspiration was standardized to exclude polymorphonuclear neutrophils and cellular debris. It minimized catabolic carryover of matrix metalloproteinases (MMP-8 and MMP-9), interleukin-1β, and Wnt-pathway antagonists, which could prematurely degrade the methacrylated gelatin network or blunt osteoblastogenesis.[29,31,32]

Phase II: bioink synthesis, biphasic bioprinting, characterization, and release assays

Porcine type A gelatin (300 Bloom) was reacted with methacrylic anhydride (0.6 mL/g gelatin) in carbonate-bicarbonate buffer (pH 9.0, 50°C, 3 hours) to achieve an 82% degree of methacrylation (GelMA). Pharmaceutical-grade unfractionated sodium heparin (15 kDa) was reacted with 2-aminoethyl methacrylate via EDC/NHS carbodiimide coupling to yield sulfated HepMA (degree of substitution 24%). Both products were dialyzed (12–14 kDa cutoff) for 7 days and lyophilized.[22,23,28] The osteogenic compartment bioink contained 10% (w/v) GelMA, 1.5% (w/v) HepMA, and 5% (w/v) silicate-substituted nanohydroxyapatite/β-tricalcium phosphate (nHAp, mean crystallite length 65 nm), dissolved in sterile PBS with 0.15% (w/v) lithium phenyl-2,4,6-trimethylbenzoylphosphinate (LAP) photoinitiator at 37°C. The softer PDL-guiding bioink comprised 7% (w/v) GelMA, 1.5% (w/v) HepMA, and 0.15% (w/v) LAP without ceramic nanoparticles.[25–27] Standardized AGF concentrate (20% v/v lyophilized-reconstituted equivalent) was pre-equilibrated with HepMA for 20 minutes at 25°C. Gentle homogenization followed. Constructs were fabricated by two-nozzle pneumatic temperature-controlled extrusion bioprinting (nozzle internal diameter 250 μm; cartridge 24°C; cooled build stage 15°C; printing speed 8.0 mm/s; pneumatic pressure 65–85 kPa) across four experimental arms (n = 6 per group): G1 (GelMA/nHAp Blank scaffold without HepMA or AGF), G2 (unmodified GelMA/nHAp scaffold with equal-dose passive bolus surface-imbibed AGF), G3 (affinity GelMA–HepMA/nHAp Blank scaffold without AGF), and G4 (personalized biphasic affinity 3DBP–HepMA–AGF bio-integrated construct).

Visible-light photopolymerization followed at 405 nm (15 mW/cm², 60 seconds).[22–24] Oscillatory and rotational rheometry quantified the power-law shear-thinning flow index (n) and storage modulus (G'). Optical micro-profilometry measured the filament printability index ($Pr = L^2/16A$) and the 3D CAD-to-print surface root-mean-square deviation (RMSD, μm). Compartment-specific compressive moduli (E_c) were determined by unconfined compression testing (1 mm/min). Gravimetric immersion in PBS and Type I collagenase (1.5 U/mL, 37°C) assessed equilibrium swelling and 28-day mass retention. Cumulative supernatant ELISA at 12 timepoints through Day 21 was fitted to Korsmeyer–Peppas release kinetics.[23,25,28]

Phase II: hPDLSC cytocompatibility, differentiation, and HUVEC angiogenesis assays

Primary human periodontal ligament stem cells (hPDLSCs, passages 3–4) were verified as $CD73^+/CD90^+/CD105^+/STRO\text{-}1^+$ and $CD34^-/CD45^-$ by flow cytometry. They were seeded onto sterilized constructs (2.0×10^5 cells/scaffold) in α-MEM supplemented with 10% fetal bovine serum and osteogenic supplements (50 μg/mL L-ascorbic acid, 10 mM β-glycerophosphate, 10 nM dexamethasone).[41–43] Viability at Day 7 was quantified by Calcein-AM/propidium iodide Live/Dead confocal z-stack imaging. Metabolic proliferation was tracked on Days 1, 3, and 7 with the Cell Counting Kit-8 (CCK-8, absorbance at 450 nm). Early osteogenic enzymatic commitment was measured at Day 14. This used the p-nitrophenyl phosphate alkaline phosphatase (ALP) assay normalized to BCA total protein (U/mg protein), while extracellular matrix calcium nodule deposition at Day 21 was quantified by cetylpyridinium chloride (CPC, 10% w/v) extraction of Alizarin Red S staining (mM Ca^{2+} equivalent).[25,27,41]

At Day 14, total RNA was extracted using TRIzol-spin columns. The RNA was then reverse-transcribed and analyzed by SYBR Green quantitative real-time

PCR (qRT-PCR, $2^{-}\Delta\Delta Ct$ normalized to GAPDH) for the osteogenic transcription factors (RUNX2, SP7/Osterix), the late bone matrix protein osteocalcin (BGLAP), angiogenic VEGFA, cementum protein-1 (CEMP1), and the periodontal ligament matricellular protein periostin (POSTN).[42–45] Paracrine angiogenic bioactivity was evaluated in parallel. Human umbilical vein endothelial cells (HUVECs, 4×10^4 cells/well) were cultured on growth-factor-reduced Matrigel in 24-hour scaffold-conditioned media, and cumulative capillary-like tube length (mm/field) and master branching nodes were quantified at 12 hours using ImageJ Angiogenesis Analyzer.[37,46]

Phase III: rat critical-size mandibular periodontal defect model and outcome assessment

Sample size was set a priori with G*Power 3.1 for a four-group fixed-effects analysis of variance. The expected effect size was f = 0.68 for the primary Week-8 bone volume fraction BV/TV. The test was two-tailed with $\alpha = 0.05$ and statistical power $1 - \beta = 0.90$. For these inputs, recalculation gives about n = 9 animals per group. The study used n = 5 animals per group per timepoint (total N = 40 healthy 12-week-old male Wistar rats, 285–315 g), which corresponds to a power of about 0.61 for f = 0.68. The primary endpoint is therefore interpreted with caution. Anesthesia was general (ketamine 75 mg/kg and xylazine 10 mg/kg intraperitoneally), with local lidocaine-epinephrine infiltration. An extraoral submandibular skin incision was made. Masseteric periosteal elevation then exposed the buccal alveolar bone over the roots of the mandibular first and second molars.[44,47] Under sterile saline irrigation, a piezoelectric micro-osteotome and a 1.0-mm round bur were used to create a standardized critical-size periodontal alveolar–PDL–cementum fenestration/crestal defect. It measured 5.0 mm mesiodistally × 3.0 mm apicocoronally × 2.0 mm buccolingually, and the buccal root cementum and superficial dentin were carefully denuded.[44,47]

Defect geometries were matched by micro-CBCT template registration. Animals were allocated by computer-generated block randomization into four arms: Group I (open flap debridement [OFD] control: surgical defect debridement and saline rinse alone), Group II (3DBP-Blank: press-fit implantation of the personalized biphasic GelMA–HepMA/nHAp scaffold without AGF), Group III (AGF-Gel: defect filling with autologous $CaCl_2$/thrombin-activated AGF fibrin gel without a 3D-printed scaffold), and Group IV (3DBP–AGF: press-fit implantation of the personalized biphasic GelMA–HepMA/nHAp construct bio-integrated with autologous AGF). Closure used layered resorbable 5-0 Vicryl. Postoperative buprenorphine analgesia followed (0.05 mg/kg subcutaneously every 12 hours for 72 hours).[40] At Week 4 (n = 20) and Week 8 (n = 20), harvested hemimandibles were scanned by high-resolution micro-CT (9-µm voxel, 70 kVp, 114 µA, 0.5-mm Al filter). The scans quantified BV/TV (%), bone mineral density (BMD, mg HA/cm³), trabecular thickness (Tb.Th, mm), trabecular number (Tb.N, mm^{-1}), trabecular separation (Tb.Sp, mm), and residual cementoenamel junction-to-alveolar bone crest vertical distance (CEJ–ABC, mm).[11,48] Decalcified EDTA paraffin sections (5 µm) were stained with hematoxylin-eosin, Masson's trichrome, and Picrosirius Red under polarized light.

The stains measured new bone area (NBA, %), new cementum thickness (NCT, µm), mean Sharpey's collagen fiber insertion angle relative to the root surface (θ_PDL, degrees), and junctional epithelial downgrowth (JED, mm). Immunohistochemistry covered CD31 microvessel density (vessels/mm²), osteocalcin (OCN % area), periostin integrated optical density (POSTN IOD), and OPG/RANKL ratio. Week-8 cardiac blood serum ALT, AST, creatinine, TNF-α, and IL-10 were also profiled for biosafety. To meet ARRIVE 2.0 requirements,[40] surgical operators created identical standardized defects. Before opening sequentially numbered, sealed opaque allocation envelopes that specified Group I–IV assignment, they inscribed a microscopic 0.2-mm apical reference notch on the denuded buccal root surface at the base of the osteotomy. The notch demarcated pre-existing cementum from de novo regenerated neocementum. After harvest, all hemimandibles were recoded with

randomized alphanumeric identifiers, so that micro-CT morphometrists, histopathologists measuring apical-notch-referenced cementum and polarized Sharpey's fiber angles, and biostatisticians remained blinded to treatment identity throughout data acquisition and statistical modeling.

Statistical analysis

Python 3.11 (SciPy 1.13 and Statsmodels 0.14) was used for all quantitative analyses, which were run by a biostatistician blinded to group allocation codes. Residual normality was checked with the Shapiro–Wilk test. Levene's test assessed homogeneity of variances. Continuous outcomes are reported as mean ± standard deviation (SD) and as median with interquartile range (IQR) in the summary tables. Multi-group comparisons in Phase II (n = 6/group) and cross-sectional Phase III timepoints (n = 5/group) were analyzed by one-way analysis of variance (ANOVA), which reported exact F-statistics, degrees of freedom, exact two-tailed p-values, partial eta-squared (η_p^2) effect sizes, Tukey's honestly significant difference (HSD) post-hoc multiplicity-adjusted pairwise p-values, and bias-corrected Hedges' g effect sizes. Phase III micro-CT and immunohistochemical outcomes at Weeks 4 and 8 (different animals at each time point; N = 40) were evaluated using a balanced two-way factorial ANOVA. The model contained the main effects of surgical Group and healing Time, plus the Group × Time interaction. Bolus-loaded G2 and affinity-sequestered G4 were compared for two-group cytokine release with two-tailed independent Student's t-tests. Pearson product-moment correlation (r) quantified mechanistic coupling across Week-8 biological endpoints (N = 20); coefficients are pooled across the four groups and are therefore descriptive. Significance was set at two-tailed $p < 0.05$. BV/TV at Week 8 was the primary endpoint, and all other endpoints are exploratory; no adjustment for multiplicity across endpoints was applied. Normality testing with the Shapiro–Wilk test has limited power at n = 5–6.

3. Results

Phase I: in silico lattice mechanobiology and heparin-affinity docking

Parametric finite element homogenization and oblique 150-N masticatory stress analysis across the three candidate open-cell scaffold architectures at matched macroporosity (67.8%–68.2%) and interconnected pore diameter (415–420 μm) indicated more favorable computed mechanical and hemodynamic performance of the TPMS Schoen Gyroid (SG) design over both Orthogonal 0°/90° Grid (OG) and Honeycomb Hexagonal (HH) topologies (Figure 1A–B; Table 1). Specifically, the SG architecture yielded a computed effective compressive modulus of 149.16 MPa with near-isotropic structural symmetry (anisotropy ratio 1.04), falling within the physiological elastic window of human cancellous alveolar bone (100–200 MPa), whereas OG (94.21 MPa; anisotropy ratio 1.68) exhibited 90° nodal stress risers producing a peak Von Mises stress of 18.60 MPa (stress-concentration factor $K_t = 2.84$; yield safety factor SF = 1.45). Eliminating orthogonal strut intersections via the zero-mean-curvature SG surface reduced the computed peak Von Mises stress by 52.8% to 8.78 MPa ($K_t = 1.34$), elevating the structural safety factor to 3.08 and yielding a simulated interfacial root-scaffold micromotion under functional loading of 12.63 μm, below the 28-μm fibrous encapsulation threshold.

Concurrently, laminar CFD perfusion modeling revealed that the continuous non-self-intersecting channels of SG increased intrinsic Darcy permeability 2.62-fold compared with OG (6.40×10^{-9} m² vs. 2.44×10^{-9} m²) and generated a uniform mean interstitial wall shear stress of 4.86 ± 0.89 mPa, placing 91.6% of the internal scaffold surface area within the 1.0–10.0 mPa osteogenic mechanotransduction zone versus only 58.4% in OG and 74.2% in HH. At the molecular scale, flexible-ligand docking and MM-GBSA rescoring across crystal structures predicted that unmodified GelMA interacts only weakly with basic growth factor surfaces (ΔG_bind ranging from −4.96 kcal/mol for TGF-β1 to −5.42 kcal/mol for PDGF-BB; micromolar

K_d = 151.64–319.86 μM; zero anionic salt bridges), consistent with the burst washout reported clinically (Figure 1C; Table 1). Conversely, covalent incorporation of sulfated HepMA was predicted to form four to five bidentate electrostatic salt bridges and seven to nine hydrogen bonds with canonical cationic Arg/Lys heparin-binding clusters, with predicted ΔG_bind values of −10.96 kcal/mol for PDGF-BB (K_d = 18.93 nM; 8,012-fold affinity gain), −10.68 kcal/mol for VEGF-A165 (K_d = 29.81 nM; 7,508-fold gain), −10.32 kcal/mol for TGF-β1 (K_d = 53.46 nM; 5,983-fold gain), and −10.54 kcal/mol for BMP-2 (K_d = 37.42 nM; 5,005-fold gain), with receptor-binding epitope geometry predicted to be preserved (backbone RMSD 0.62–0.71 Å).

Table 1. Phase I In Silico Biomechanical Finite Element Homogenization, CFD Perfusion Mechanobiology, and Heparin-Affinity Molecular Docking Energetics.

Candidate Architecture / Cytokine	Structural / Crystal Specification	Primary Metric I	Primary Metric II	Interfacial Transport / Bonding	Mechanobiological / Affinity Outcome
Panel A: 3D Lattice FEA & Perfusion	Porosity φ (%) / Pore Ø (μm)	Effective E* (MPa) / Anisotropy	Peak σ_VM (MPa) / Safety Factor	Darcy k (×10^{-9} m²) / Mean WSS	Osteogenic WSS Zone (%) / Micromotion
Orthogonal 0°/90° Grid (OG)	67.8% / 415 μm	94.21 MPa / 1.68	18.60 MPa / SF = 1.45	2.44 / 2.14 ± 1.48 mPa	58.4% / 20.00 μm
Honeycomb Hexagonal (HH)	68.1% / 418 μm	118.88 MPa / 1.36	13.43 MPa / SF = 2.01	3.74 / 3.28 ± 1.21 mPa	74.2% / 15.85 μm
TPMS Schoen Gyroid (SG)	68.2% / 420 μm	149.16 MPa / 1.04	8.78 MPa / SF = 3.08	6.40 / 4.86 ± 0.89 mPa	91.6% / 12.63 μm
Panel B: Crystal Heparin Docking	RCSB PDB ID / HBD Motif	Unmodified GelMA ΔG (K_d)	Sulfated GelMA–HepMA ΔG (K_d)	H-Bonds / SO_3^- Salt Bridges	Affinity Fold Gain / Epitope RMSD
PDGF-BB	3MJG (Arg27, Arg28, Asn54, Lys80, Lys81, Arg82)	−5.42 kcal/mol (151.64 μM)	−10.96 kcal/mol (18.93 nM)	9 H-bonds / 5 salt bridges	8,012× gain / RMSD 0.62 Å
VEGF-A165	3V2A (Arg123, Arg124, Lys125, Lys140, Arg145, Arg159)	−5.18 kcal/mol (223.84 μM)	−10.68 kcal/mol (29.81 nM)	8 H-bonds / 5 salt bridges	7,508× gain / RMSD 0.68 Å
TGF-β1	3KFD (Arg25, Lys26, Lys31, His34, Arg94, Lys97)	−4.96 kcal/mol (319.86 μM)	−10.32 kcal/mol (53.46 nM)	7 H-bonds / 4 salt bridges	5,983× gain / RMSD 0.71 Å
BMP-2	1REW (Lys5, Arg7, Lys8, Arg9, Arg11, Lys15)	−5.29 kcal/mol (187.25 μM)	−10.54 kcal/mol (37.42 nM)	8 H-bonds / 4 salt bridges	5,005× gain / RMSD 0.65 Å

Finite element simulations solved under an oblique 150-N (30°) mandibular molar masticatory load; osteogenic wall shear stress (WSS) window defined as $\tau_w \in [1.0, 10.0]$ mPa; interfacial osseointegration micromotion threshold < 28 μm. Molecular docking & MM-GBSA free energies evaluated at T = 310.15 K (RT = 0.6163 kcal/mol). Abbreviations: HBD, heparin-binding domain; K_d, equilibrium dissociation constant; RMSD, root-mean-square deviation; SF, yield safety factor; TPMS, triply periodic minimal surface. Stress-concentration factors (text): K_t = 2.84 (OG) and 1.34 (SG). Binding energies and K_d values are computational predictions (docking with MM-GBSA rescoring).

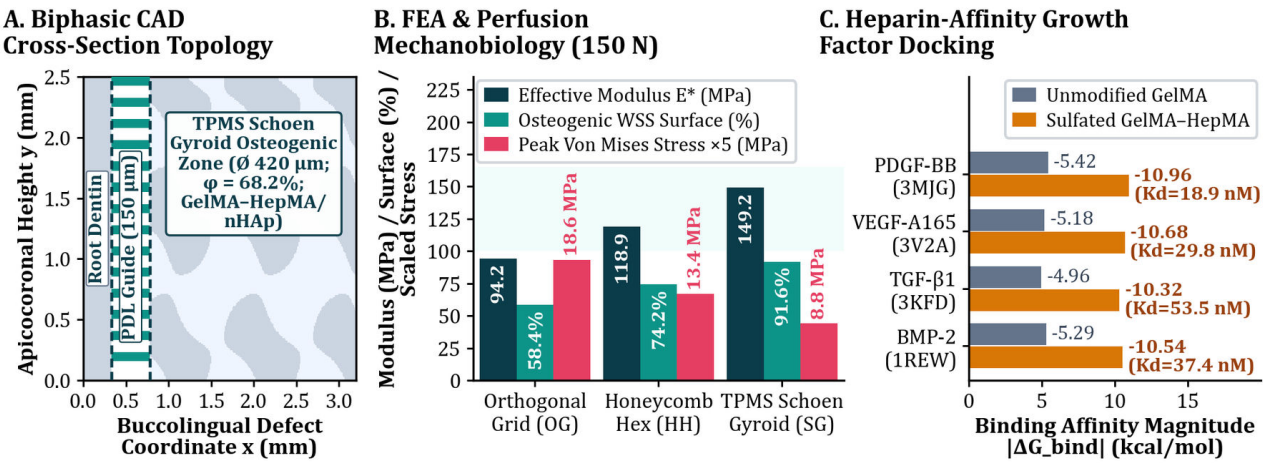

Figure 1. Phase I in silico optimization of biphasic scaffold mechanobiology and heparin-affinity morphogen sequestration. (A) Parametric two-dimensional cross-section of the personalized CBCT-matched construct depicting the root-facing 150-µm micro-grooved GelMA–HepMA periodontal ligament (PDL) guidance interface and the outer triply periodic minimal surface (TPMS) Schoen Gyroid osteogenic compartment (Ø 420 µm; porosity φ = 68.2%). (B) Finite element analysis (150 N oblique 30° molar load) and laminar computational fluid dynamics perfusion comparison across Orthogonal Grid (OG), Honeycomb Hexagonal (HH), and TPMS Schoen Gyroid (SG) topologies. (C) Molecular docking binding free energies (|ΔG_bind|) and predicted nanomolar dissociation constants (K_d) of PDGF-BB (3MJG), VEGF-A165 (3V2A), TGF-β1 (3KFD), and BMP-2 (1REW) against unmodified GelMA versus sulfated GelMA–HepMA networks.

Table 2. Phase II Rheological Printability, Biphasic Mechanical Stratification, Biostability, and 21-Day Autologous AGF Release Kinetics (N = 24 Constructs; n = 6/Group).

Physicochemical / Release Parameter	G1: GelMA/nHAp Blank (n = 6)	G2: GelMA/nHAp + Bolus AGF (n = 6)	G3: GelMA–HepMA/ nHAp Blank (n = 6)	G4: 3DBP–HepMA– AGF (n = 6)	ANOVA F(3,20) / t(10) & Effect	p-value
Shear-Thinning Flow Index (n)	0.39 ± 0.02 [0.40; 0.39–0.40]	0.38 ± 0.02 [0.38; 0.37–0.40]	0.34 ± 0.02 [0.34; 0.33–0.34]	0.33 ± 0.016 [0.33; 0.32–0.34]	F = 15.07 (η_p² = 0.693)	< 0.001*
Storage Modulus G' (kPa)	14.8 ± 1.1 [15.0; 14.0–15.7]	14.5 ± 1.2 [14.4; 14.3–15.0]	18.6 ± 1.3 [18.5; 18.2–19.2]	19.2 ± 1.2 [19.1; 18.5–20.0]	F = 25.31 (η_p² = 0.792)	< 0.001*
Filament Printability Index (Pr)	0.94 ± 0.03 [0.94; 0.91–0.96]	0.93 ± 0.03 [0.93; 0.92–0.94]	0.98 ± 0.02 [0.98; 0.97–0.99]	0.99 ± 0.02 [0.99; 0.98–1.00]	F = 8.00 (η_p² = 0.545)	0.0011*
3D CAD-to-Print Surface RMSD (µm)	96.4 ± 8.5 [99.9; 90.9–101.7]	99.2 ± 9.1 [100.3; 94.1–104.0]	74.8 ± 6.4 [74.3; 72.3–78.2]	72.5 ± 5.8 [72.6; 68.4–76.9]	F = 20.54 (η_p² = 0.755)	< 0.001*
Osteogenic Zone Modulus E_osteo (kPa)	142.5 ± 10.4 [145.7; 134.8–150.8]	139.8 ± 11.2 [137.0; 132.9–144.3]	176.4 ± 11.8 [177.7; 170.3–186.0]	182.6 ± 12.1 [179.2; 175.8–180.5]	F = 23.01 (η_p² = 0.775)	< 0.001*
PDL-Guiding Zone Modulus E_PDL (kPa)	19.4 ± 1.8 [19.8; 18.0–20.9]	19.1 ± 1.9 [19.1; 18.0–20.6]	21.8 ± 1.7 [21.5; 21.1–21.7]	22.4 ± 1.6 [22.4; 22.3–22.5]	F = 5.43 (η_p² = 0.449)	0.0068*
Equilibrium Swelling Ratio (%)	342.0 ± 18.0 [341.8; 333.4–348.3]	348.0 ± 20.0 [346.7; 337.8–358.4]	286.0 ± 15.0 [280.9; 277.3–289.5]	279.0 ± 14.0 [283.7; 268.1–290.1]	F = 27.59 (η_p² = 0.805)	< 0.001*
Day-28 Collagenase Mass Retention (%)	41.2 ± 3.6 [41.5; 39.8–43.8]	39.5 ± 3.8 [39.6; 36.8–42.7]	61.8 ± 3.4 [62.4; 60.2–63.7]	64.2 ± 3.1 [65.9; 62.2–66.4]	F = 85.21 (η_p² = 0.927)	< 0.001*
24-h PDGF-BB Burst Release (%)	N/A (Unloaded)	79.4 ± 4.2 [80.8; 79.3–81.3]	N/A (Unloaded)	19.8 ± 2.1 [19.6; 17.9–21.5]	t = −31.09 (g = −16.57)	< 0.001*
24-h VEGF-A165 Burst Release (%)	N/A (Unloaded)	75.8 ± 3.9 [76.8; 74.6–78.7]	N/A (Unloaded)	18.4 ± 1.9 [18.3; 17.4–19.7]	t = −32.41 (g = −17.27)	< 0.001*
24-h TGF-β1 Burst Release (%)	N/A (Unloaded)	72.6 ± 4.1 [72.0; 70.9–72.7]	N/A (Unloaded)	17.2 ± 1.8 [16.8; 16.1–17.4]	t = −30.31 (g = −16.15)	< 0.001*

Physicochemical / Release Parameter	G1: GelMA/nHAp Blank (n = 6)	G2: GelMA/nHAp + Bolus AGF (n = 6)	G3: GelMA–HepMA/ nHAp Blank (n = 6)	G4: 3DBP–HepMA– AGF (n = 6)	ANOVA F(3,20) / t(10) & Effect	p-value
Day-21 Cumulative PDGF-BB Release (%)	N/A (Unloaded)	96.2 ± 1.8 [96.4; 94.5–97.8]	N/A (Unloaded)	84.6 ± 2.9 [85.4; 83.4–85.5]	t = −8.32 (g = −4.44)	< 0.001*

Values reported as mean ± SD [median; IQR]. *Statistically significant at two-tailed $p < 0.05$ via one-way ANOVA ($F(3,20)$) for 4-group biomaterial metrics or independent Student's t-test ($df = 10$) comparing AGF-loaded G4 versus bolus G2. Baseline cell-free autologous AGF concentrate (n = 6 batches): platelets 1,205.3 ± 78.0 × 10^3/μL (4.86 ± 0.24× enrichment), PDGF-BB 14,820.0 ± 940.0 pg/mL, VEGF-A165 2,860.0 ± 215.0 pg/mL, TGF-β1 38,450.0 ± 2,410.0 pg/mL, and IGF-1 94.6 ± 7.2 ng/mL.

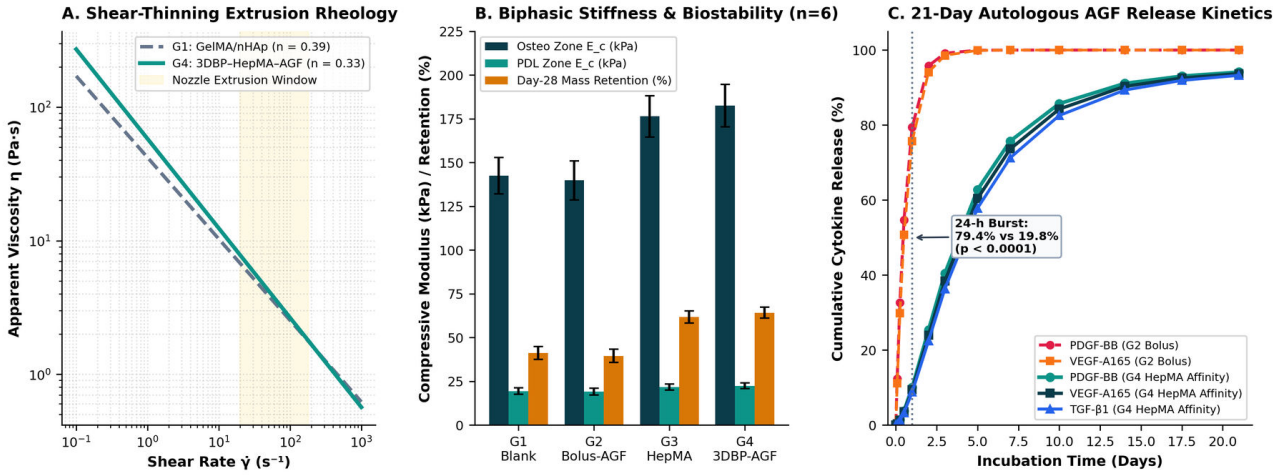

Figure 2. Phase II bioink extrusion rheology, biphasic mechanical stratification, and 21-day autologous AGF release kinetics (n = 6 constructs/group). (A) Log–log power-law shear-thinning apparent viscosity curves across pneumatic nozzle shear rates. (B) Unconfined compressive moduli of the nHAp-reinforced osteogenic compartment versus the soft PDL-guiding compartment alongside Day-28 collagenase mass retention. (C) Cumulative 21-day cytokine release trajectories comparing passive bolus-loaded GelMA/nHAp (G2) rapid 24-hour burst washout against sustained Korsmeyer–Peppas affinity release from bio-integrated 3DBP–HepMA–AGF (G4).

Phase II: bioink rheology, printability, mechanical stratification, and AGF release kinetics

Hematological and ELISA quality control across six independent autologous preparations confirmed reproducible 4.86 ± 0.24-fold platelet enrichment from whole blood (1,205.3 ± 78.0 × 10^3/μL vs. 248.0 ± 21.0 × 10^3/μL), yielding high-titer cell-free AGF concentrates containing 14,820.0 ± 940.0 pg/mL PDGF-BB, 2,860.0 ± 215.0 pg/mL VEGF-A165, 38,450.0 ± 2,410.0 pg/mL TGF-β1, and 94.6 ± 7.2 ng/mL IGF-1. Across the four bioprinted experimental formulations (N = 24 constructs; n = 6/group), dual-network GelMA–HepMA/nHAp bioinks exhibited non-Newtonian shear-thinning behavior suited to low-shear pneumatic extrusion, with flow behavior indices decreasing significantly (more pronounced shear thinning) from 0.39 ± 0.020 in G1 to 0.33 ± 0.016 in bio-integrated G4 (ANOVA $F(3,20) = 15.07$, $p < 0.001$, $\eta_p^2 = 0.693$; Figure 2A; Table 2). Following 405-nm LAP photocrosslinking, HepMA interpenetration and polyvalent growth factor bridging increased storage modulus G' from 14.8 ± 1.1 kPa (G1) to 19.2 ± 1.2 kPa (G4; $F(3,20) = 25.31$, $p < 0.001$), elevating filament printability index Pr to near-ideal square pore fidelity (0.99 ± 0.02 vs. 0.94 ± 0.03 in G1; $p = 0.0011$) and reducing 3D optical CAD-to-print surface RMSD deviation by 24.8% from 96.4 ± 8.5 μm to 72.5 ± 5.8 μm ($F(3,20) = 20.54$, $p < 0.001$).

Unconfined compression testing showed distinct compartmentalized mechanical stratification within the monolithic G4 construct: the nHAp-reinforced gyroid osteogenic zone reached 182.6 ± 12.1 kPa (vs.

142.5 ± 10.4 kPa in G1; $p < 0.001$), whereas the nanoparticle-free micro-grooved PDL interface maintained a compliant extracellular-matrix-mimetic modulus of 22.4 ± 1.6 kPa (Figure 2B). Furthermore, HepMA conjugation moderated equilibrium swelling from 342.0 ± 18.0% (G1) to 279.0 ± 14.0% (G4; $p < 0.001$) and increased 28-day collagenase mass retention from 41.2 ± 3.6% to 64.2 ± 3.1% ($F(3,20) = 85.21$, $p < 0.001$). The 21-day ELISA release profiling showed sustained release consistent with the Phase I reaction-diffusion model: passively imbibed G2 scaffolds showed a 24-hour burst washout of 79.4 ± 4.2% for PDGF-BB, 75.8 ± 3.9% for VEGF-A165, and 72.6 ± 4.1% for TGF-β1, exhausting >95% of soluble payload within 96 hours, whereas affinity-engineered G4 constructs curtailed 24-hour burst release fourfold to 19.8 ± 2.1% for PDGF-BB ($t = -31.09$, $p < 0.001$), 18.4 ± 1.9% for VEGF-A165 ($p < 0.001$), and 17.2 ± 1.8% for TGF-β1 ($p < 0.001$), sustaining controlled delivery totaling 84.6 ± 2.9% through Day 21 (Figure 2C; Table 2). Nonlinear regression of the 21-day cumulative release profiles to the Korsmeyer–Peppas power-law model ($M_t/M_\infty = k_{KP} \cdot t^n$) yielded diffusional release exponents of $n_{KP} = 0.46 \pm 0.03$ for PDGF-BB ($R^2 = 0.994$), 0.45 ± 0.02 for VEGF-A165 ($R^2 = 0.995$), and 0.47 ± 0.03 for TGF-β1 ($R^2 = 0.993$) in G4 constructs, indicating release close to the Fickian diffusion limit, with a possible minor contribution from slow cell-/collagenase-mediated hydrogel relaxation, rather than uncontrolled burst release.

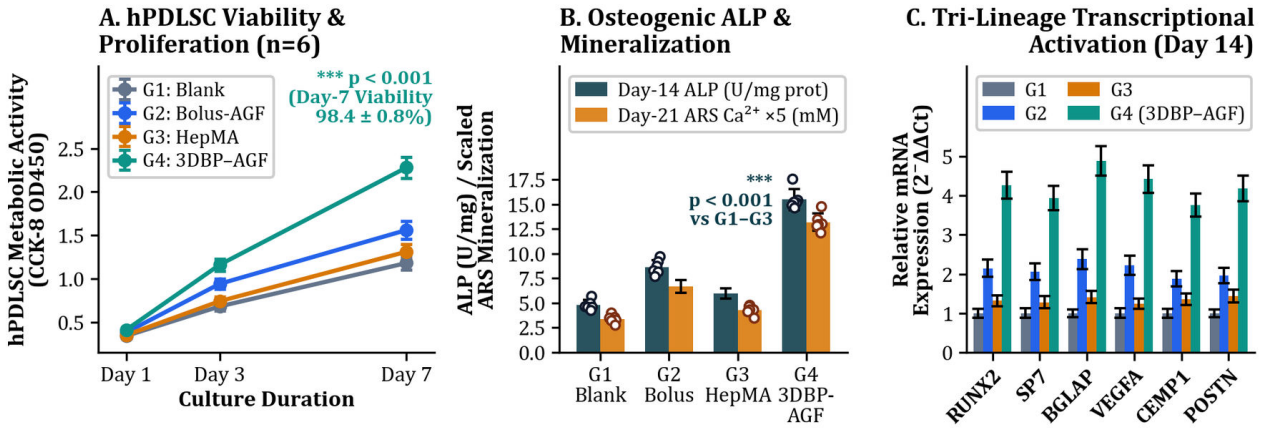

Figure 3. Phase II in vitro cytocompatibility, osteo-cementogenic differentiation of human periodontal ligament stem cells (hPDLSCs), and endothelial tubulogenesis (N = 24; n = 6/group). (A) Longitudinal CCK-8 metabolic proliferation (Days 1, 3, and 7) and Day-7 Live/Dead viability. (B) Day-14 alkaline phosphatase (ALP) enzymatic activity and Day-21 CPC-extracted Alizarin Red S calcium mineralization with replicate-level scatter. (C) Day-14 quantitative RT-PCR relative mRNA expression ($2^{-}\Delta\Delta Ct$) of osteogenic (RUNX2, SP7, BGLAP), angiogenic (VEGFA), cementogenic (CEMP1), and ligamentous matricellular (POSTN) markers.

Table 3. Phase II In Vitro hPDLSC Cytocompatibility, Osteo-Cementogenic Differentiation, Transcriptional Profiling, and HUVEC Angiogenesis (N = 24; n = 6/Group).

Cellular / Molecular Endpoint	G1: GelMA/nHAp Blank (n = 6)	G2: GelMA/nHAp + Bolus AGF (n = 6)	G3: GelMA–HepMA/ nHAp Blank (n = 6)	G4: 3DBP–HepMA– AGF (n = 6)	ANOVA F(3,20) & Hedges' g (G4 vs G2)	p-value
Day-7 Live/Dead Cell Viability (%)	94.2 ± 1.4 [93.6; 93.2–95.1]	95.8 ± 1.3 [95.2; 95.0–96.7]	95.4 ± 1.2 [95.3; 94.6–96.5]	98.4 ± 0.8 [98.5; 97.9–99.0]	F = 13.11 (g_4v2 = 2.22)	< 0.001*
Day-1 CCK-8 Proliferation (OD450)	0.34 ± 0.03 [0.34; 0.33–0.35]	0.38 ± 0.03 [0.36; 0.36–0.40]	0.35 ± 0.03 [0.34; 0.33–0.36]	0.41 ± 0.03 [0.41; 0.40–0.43]	F = 6.67 (g_4v2 = 0.92)	0.0027*

Cellular / Molecular Endpoint	G1: GelMA/nHAp Blank (n = 6)	G2: GelMA/nHAp + Bolus AGF (n = 6)	G3: GelMA–HepMA/ nHAp Blank (n = 6)	G4: 3DBP–HepMA– AGF (n = 6)	ANOVA F(3,20) & Hedges' g (G4 vs G2)	p-value
Day-3 CCK-8 Proliferation (OD450)	0.68 ± 0.05 [0.69; 0.67–0.72]	0.94 ± 0.06 [0.94; 0.90–0.98]	0.74 ± 0.05 [0.74; 0.70–0.77]	1.16 ± 0.07 [1.13; 1.12–1.18]	F = 83.91 (g_4v2 = 3.12)	< 0.001*
Day-7 CCK-8 Proliferation (OD450)	1.18 ± 0.08 [1.16; 1.12–1.22]	1.56 ± 0.10 [1.55; 1.50–1.58]	1.31 ± 0.09 [1.32; 1.27–1.34]	2.28 ± 0.12 [2.30; 2.22–2.36]	F = 148.75 (g_4v2 = 6.02)	< 0.001*
Day-14 ALP Activity (U/mg protein)	4.82 ± 0.48 [4.67; 4.60–4.92]	8.64 ± 0.72 [8.52; 8.21–9.09]	5.96 ± 0.54 [5.67; 5.65–6.05]	15.48 ± 1.06 [15.17; 14.97–15.36]	F = 253.35 (g_4v2 = 6.97)	< 0.001*
Day-21 ARS Mineralization (mM Ca^{2+})	0.68 ± 0.08 [0.68; 0.66–0.71]	1.34 ± 0.13 [1.30; 1.28–1.33]	0.86 ± 0.09 [0.87; 0.84–0.92]	2.64 ± 0.18 [2.60; 2.57–2.68]	F = 294.62 (g_4v2 = 7.64)	< 0.001*
Day-14 RUNX2 mRNA ($2^{-}\Delta\Delta Ct$ fold)	1.00 ± 0.11 [0.97; 0.94–1.00]	2.14 ± 0.22 [2.16; 2.08–2.20]	1.32 ± 0.14 [1.36; 1.33–1.40]	4.26 ± 0.34 [4.33; 4.01–4.40]	F = 264.08 (g_4v2 = 6.83)	< 0.001*
Day-14 SP7 / Osterix mRNA (fold)	1.00 ± 0.12 [0.96; 0.95–1.07]	2.06 ± 0.21 [2.04; 1.90–2.16]	1.28 ± 0.15 [1.29; 1.22–1.35]	3.94 ± 0.31 [3.92; 3.71–4.07]	F = 237.88 (g_4v2 = 6.55)	< 0.001*
Day-14 BGLAP / Osteocalcin mRNA (fold)	1.00 ± 0.10 [1.01; 0.95–1.05]	2.38 ± 0.25 [2.41; 2.23–2.50]	1.41 ± 0.16 [1.42; 1.32–1.46]	4.88 ± 0.38 [4.82; 4.60–4.97]	F = 299.87 (g_4v2 = 7.17)	< 0.001*
Day-14 VEGFA mRNA (fold)	1.00 ± 0.12 [1.01; 0.92–1.10]	2.22 ± 0.24 [2.35; 2.06–2.38]	1.24 ± 0.13 [1.23; 1.14–1.31]	4.42 ± 0.35 [4.38; 4.23–4.65]	F = 275.83 (g_4v2 = 6.77)	< 0.001*
Day-14 CEMP1 mRNA (fold)	1.00 ± 0.11 [1.00; 0.94–1.06]	1.88 ± 0.19 [1.84; 1.78–1.89]	1.36 ± 0.15 [1.38; 1.27–1.42]	3.76 ± 0.29 [3.69; 3.65–3.92]	F = 233.67 (g_4v2 = 7.08)	< 0.001*
Day-14 POSTN / Periostin mRNA (fold)	1.00 ± 0.10 [1.02; 0.95–1.06]	1.96 ± 0.20 [2.01; 1.86–2.07]	1.44 ± 0.16 [1.44; 1.31–1.52]	4.18 ± 0.32 [4.26; 4.15–4.38]	F = 268.92 (g_4v2 = 7.68)	< 0.001*
HUVEC Tube Length (mm/field)	3.42 ± 0.38 [3.29; 3.13–3.76]	6.85 ± 0.62 [6.65; 6.39–7.09]	3.96 ± 0.42 [4.04; 3.68–4.29]	12.14 ± 0.84 [12.16; 11.54–12.44]	F = 271.26 (g_4v2 = 6.61)	< 0.001*
HUVEC Master Branching Nodes/field	14.2 ± 2.1 [14.2; 12.9–15.4]	31.6 ± 3.4 [32.3; 30.2–33.4]	17.4 ± 2.3 [17.0; 15.7–17.9]	58.8 ± 4.5 [58.6; 55.8–62.7]	F = 238.86 (g_4v2 = 6.30)	< 0.001*

Values expressed as mean ± SD [median; IQR]. *All pairwise Tukey HSD comparisons between G4 (3DBP–HepMA–AGF) and G1, G2, and G3 were statistically significant at adjusted $p < 0.001$ (except Day-1 CCK-8 G4 vs. G2 adjusted $p = 0.348$). Abbreviations: ALP, alkaline phosphatase; ARS, Alizarin Red S cetylpyridinium chloride extraction; hPDLSC, human periodontal ligament stem cell; HUVEC, human umbilical vein endothelial cell.

Phase II: in vitro hPDLSC cytocompatibility, osteo-cementogenic commitment, and endothelial tubulogenesis

Confocal Live/Dead imaging at Day 7 showed high cytocompatibility across all four bioprinted groups (>94% viable spindle-shaped hPDLSCs), with bio-integrated G4 constructs achieving the highest viability of 98.4 ± 0.8% compared with 94.2 ± 1.4% in G1, 95.8 ± 1.3% in bolus G2, and 95.4 ± 1.2% in HepMA-blank G3 (ANOVA $F(3,20) = 13.11$, $p < 0.001$, $\eta_p^2 = 0.663$; Figure 3A; Table 3). Serial CCK-8 metabolic assays revealed progressively increasing group differences in proliferation from Day 1 ($p = 0.0027$) through Day 3 (1.16 ± 0.07 in G4 vs. 0.68 ± 0.05 in G1; $p < 0.001$) and Day 7, at which point G4 reached an OD450 of 2.28 ± 0.12, representing a 1.93-fold expansion over G1 (1.18 ± 0.08) and a 1.46-fold gain over bolus-loaded G2 (1.56 ± 0.10; Tukey HSD $p < 0.0001$; Hedges' $g = 6.02$), which is consistent with the interpretation that sustained cytokine retention may limit loss of mitogenic stimulation after culture media exchanges (cytokine retention was not measured in this assay).

Early osteogenic differentiation assessed by Day-14 ALP enzymatic activity increased 3.21-fold in G4 (15.48 ± 1.06 U/mg protein) relative to G1 (4.82 ± 0.48 U/mg) and 1.79-fold relative to G2 (8.64 ± 0.72 U/mg; $F(3,20) = 253.35$, $p < 0.001$, $\eta_p^2 = 0.974$; Figure 3B). Similarly, Day-21 CPC-extracted Alizarin Red S mineralization showed dense calcified extracellular nodule deposition in G4 (2.64 ± 0.18 mM Ca^{2+}), nearly

doubling bolus G2 (1.34 ± 0.13 mM) and quadrupling G1 (0.68 ± 0.08 mM; $F(3,20) = 294.62$, $p < 0.001$). At the transcriptional level on Day 14, qRT-PCR showed coordinated upregulation in G4 across master osteogenic regulators RUNX2 (4.26 ± 0.34-fold vs. 2.14 ± 0.22-fold in G2; $p < 0.001$), SP7/Osterix (3.94 ± 0.31-fold), and late osteocalcin BGLAP (4.88 ± 0.38-fold), simultaneously accompanied by elevated cementogenic marker CEMP1 (3.76 ± 0.29-fold vs. 1.88 ± 0.19-fold in G2), PDL tenogenic-matricellular marker POSTN (4.18 ± 0.32-fold), and endogenous angiogenic VEGFA (4.42 ± 0.35-fold; all ANOVA $p < 0.001$; Figure 3C; Table 3).

Functional HUVEC Matrigel tubulogenesis assays corroborated these transcriptomic gains: conditioned medium from Day-7 G4 scaffolds induced interconnected capillary networks measuring 12.14 ± 0.84 mm/field with 58.8 ± 4.5 master branching nodes, exceeding bolus G2 (6.85 ± 0.62 mm/field; 31.6 ± 3.4 nodes) and blank controls ($p < 0.001$).

Phase III: micro-CT alveolar bone morphometry at Weeks 4 and 8

All 40 operated male Wistar rats survived the surgical procedure and postoperative observation periods through Weeks 4 and 8 without wound dehiscence, scaffold extrusion, purulent infection, or masticatory weight loss. High-resolution three-dimensional micro-CT reconstructions revealed differences between time points (independent animals were assessed at Weeks 4 and 8) in de novo mineralized tissue bridging across the critical-size 5.0 × 3.0 × 2.0 mm mandibular alveolar defect (Figure 4A–C; Table 4). At Week 4, OFD negative controls (Group I) exhibited minimal peripheral bone repair restricted to the osteotomy margins (BV/TV = 14.6 ± 2.2%; BMD = 318.0 ± 24.0 mg HA/cm³), consistent with the non-spontaneous healing of a critical-size defect. Both personalized blank scaffolds (Group II: BV/TV = 28.4 ± 2.9%) and standalone autologous AGF fibrin gels (Group III: BV/TV = 26.8 ± 3.1%) doubled early bone volume relative to OFD (Tukey HSD $p < 0.001$), whereas personalized bio-integrated 3DBP–AGF constructs (Group IV) achieved 48.6 ± 3.5% BV/TV and 624.0 ± 33.0 mg HA/cm³ BMD already by Week 4 (ANOVA $F(3,16) = 113.03$, $p < 0.001$, $\eta_p^2 = 0.955$). By Week 8, a difference emerged between scaffold-only Group II and scaffoldless AGF-Gel Group III: possibly because of mucoperiosteal flap compression and fibrin fibrinolysis (not measured), Group III plateaued at 41.2 ± 4.1% BV/TV, falling significantly behind space-maintaining Group II (51.8 ± 3.8%; Tukey $p = 0.0018$), while bio-integrated Group IV reached 76.4 ± 3.9% BV/TV and 846.0 ± 35.0 mg HA/cm³ BMD (Week-8 ANOVA $F(3,16) = 186.94$, $p < 0.001$, $\eta_p^2 = 0.972$; Hedges' $g = 14.33$ vs. Group I, $g = 5.79$ vs. Group II, and $g = 7.93$ vs. Group III).

Two-way factorial ANOVA across all 40 animals showed significant Group × Time interactions for BV/TV ($F(3,32) = 18.02$, $p < 0.001$, $\eta_p^2 = 0.628$), BMD ($F(3,32) = 8.41$, $p < 0.001$), and trabecular thickness Tb.Th ($F(3,32) = 12.54$, $p < 0.001$; Table 5), which indicates that group differences widened between Week 4 and Week 8. At Week 8, Group IV showed dense, plate-like trabeculae (Tb.Th = 0.274 ± 0.015 mm; Tb.N = 4.36 ± 0.28 mm^{-1}; Tb.Sp = 0.142 ± 0.016 mm) and restored the alveolar crest to within 0.64 ± 0.08 mm of the cementoenamel junction, close to the value of about 0.53 mm reported for healthy control rats,[49] compared with a 2.34 ± 0.15 mm residual vertical defect in OFD controls ($p < 0.001$). Additivity was evaluated at Week 8: relative to the OFD negative-control baseline (22.4% BV/TV), standalone structural bioprinting in Group II contributed a net gain of +29.4 percentage points (to 51.8%) and standalone autologous AGF gel in Group III contributed +18.8 percentage points (to 41.2%), yielding an expected additive benchmark of +48.2 percentage points (70.6% BV/TV). Bio-integrated Group IV (3DBP–AGF) achieved a net gain of +54.0 percentage points above OFD (reaching 76.4 ± 3.9% BV/TV).

Group IV exceeded either component alone and numerically exceeded the additive benchmark (76.4% vs. 70.6% expected). The additive contrast (Group IV − II − III + I), calculated from the reported means and SDs with pooled error (16 df), was +8.0 percentage

points at Week 4 (SE 2.65; 95% CI 2.4 to 13.6; p = 0.008) and +5.8 percentage points at Week 8 (SE 3.30; 95% CI −1.2 to 12.8; p = 0.098). Supra-additivity was therefore statistically supported at Week 4 but not at Week 8.

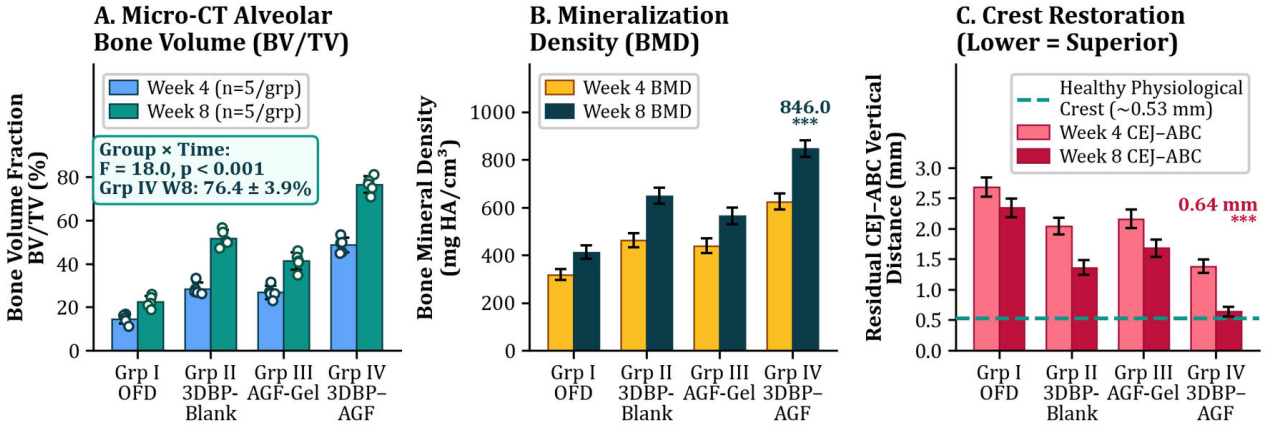

Figure 4. Phase III longitudinal three-dimensional micro-CT alveolar bone morphometry in critical-size (5.0 × 3.0 × 2.0 mm) rat mandibular periodontal defects at Weeks 4 and 8 (N = 40; n = 5/group/timepoint). (A) Bone volume fraction (BV/TV, %) with individual animal replicates and two-way ANOVA Group × Time interaction statistics. (B) Bone mineral density (BMD, mg HA/cm³). (C) Residual cementoenamel junction-to-alveolar bone crest (CEJ–ABC) vertical defect height relative to the physiological alveolar crest (~0.53 mm in healthy control rats).

Table 4. Phase III Longitudinal Three-Dimensional Micro-CT Alveolar Bone Morphometry at Weeks 4 and 8 Post-Surgery (N = 40 Wistar Rats; n = 5/Group/Timepoint).

Micro-CT Parameter & Timepoint	Group I: OFD Control (n = 5)	Group II: 3DBP- Blank (n = 5)	Group III: Autologous AGF-Gel (n = 5)	Group IV: Personalized 3DBP–AGF (n = 5)	One-Way ANOVA F(3,16) & η_p²	p-value
Bone Volume Fraction BV/TV (%), Week 4	14.6 ± 2.2 [14.9; 13.8–16.4]	28.4 ± 2.9 [27.2; 26.9–28.3]	26.8 ± 3.1 [26.1; 26.1–27.1]	48.6 ± 3.5 [49.6; 45.4–49.7]	F = 113.03 (η_p² = 0.955)	< 0.001*
Bone Volume Fraction BV/TV (%), Week 8	22.4 ± 2.8 [21.8; 21.2–24.4]	51.8 ± 3.8 [50.4; 50.1–54.6]	41.2 ± 4.1 [41.3; 40.7–43.2]	76.4 ± 3.9 [76.9; 75.0–78.2]	F = 186.94 (η_p² = 0.972)	< 0.001*
Bone Mineral Density BMD (mg HA/cm³), Week 4	318.0 ± 24.0 [309.7; 304.3–314.6]	462.0 ± 29.0 [462.2; 434.5–488.6]	438.0 ± 31.0 [448.2; 414.8–460.7]	624.0 ± 33.0 [640.9; 598.4–645.9]	F = 91.43 (η_p² = 0.945)	< 0.001*
Bone Mineral Density BMD (mg HA/cm³), Week 8	412.0 ± 28.0 [415.5; 410.5–420.3]	648.0 ± 34.0 [652.2; 632.8–652.5]	564.0 ± 36.0 [570.7; 530.3–590.2]	846.0 ± 35.0 [839.3; 827.4–849.7]	F = 146.81 (η_p² = 0.965)	< 0.001*
Trabecular Thickness Tb.Th (mm), Week 4	0.088 ± 0.009 [0.090; 0.087–0.094]	0.132 ± 0.011 [0.137; 0.125–0.139]	0.124 ± 0.012 [0.129; 0.111–0.132]	0.186 ± 0.013 [0.191; 0.176–0.194]	F = 63.62 (η_p² = 0.923)	< 0.001*
Trabecular Thickness Tb.Th (mm), Week 8	0.112 ± 0.010 [0.112; 0.106–0.118]	0.194 ± 0.014 [0.196; 0.187–0.202]	0.162 ± 0.015 [0.158; 0.157–0.170]	0.274 ± 0.015 [0.269; 0.262–0.286]	F = 123.85 (η_p² = 0.959)	< 0.001*
Trabecular Number Tb.N (mm⁻¹), Week 4	1.64 ± 0.18 [1.60; 1.51–1.74]	2.36 ± 0.22 [2.33; 2.21–2.33]	2.24 ± 0.24 [2.29; 2.03–2.38]	3.42 ± 0.26 [3.35; 3.31–3.57]	F = 53.21 (η_p² = 0.909)	< 0.001*
Trabecular Number Tb.N (mm⁻¹), Week 8	2.02 ± 0.21 [1.94; 1.88–2.24]	3.18 ± 0.25 [3.04; 3.01–3.32]	2.78 ± 0.27 [2.83; 2.62–2.87]	4.36 ± 0.28 [4.48; 4.10–4.56]	F = 73.98 (η_p² = 0.933)	< 0.001*
Trabecular Separation Tb.Sp (mm), Week 4	0.542 ± 0.038 [0.557; 0.521–0.558]	0.368 ± 0.029 [0.369; 0.343–0.389]	0.392 ± 0.032 [0.410; 0.368–0.414]	0.228 ± 0.021 [0.230; 0.212–0.239]	F = 88.20 (η_p² = 0.943)	< 0.001*
Trabecular Separation Tb.Sp (mm), Week 8	0.456 ± 0.035 [0.465; 0.460–0.465]	0.258 ± 0.024 [0.251; 0.248–0.266]	0.312 ± 0.028 [0.314; 0.294–0.329]	0.142 ± 0.016 [0.140; 0.129–0.150]	F = 119.56 (η_p² = 0.957)	< 0.001*

Micro-CT Parameter & Timepoint	Group I: OFD Control (n = 5)	Group II: 3DBP- Blank (n = 5)	Group III: Autologous AGF-Gel (n = 5)	Group IV: Personalized 3DBP–AGF (n = 5)	One-Way ANOVA F(3,16) & η_p²	p-value
Residual CEJ–ABC Defect Height (mm), Week 4	2.68 ± 0.16 [2.67; 2.59–2.72]	2.04 ± 0.14 [2.04; 1.99–2.13]	2.16 ± 0.15 [2.15; 2.07–2.18]	1.38 ± 0.11 [1.34; 1.33–1.37]	F = 71.60 (η_p² = 0.931)	< 0.001*
Residual CEJ–ABC Defect Height (mm), Week 8	2.34 ± 0.15 [2.39; 2.33–2.40]	1.36 ± 0.12 [1.32; 1.29–1.36]	1.68 ± 0.14 [1.61; 1.57–1.82]	0.64 ± 0.08 [0.65; 0.60–0.68]	F = 158.68 (η_p² = 0.967)	< 0.001*

Values expressed as mean ± SD [median; IQR] across n = 5 independent hemimandibles per surgical group at each endpoint. *Statistically significant via one-way ANOVA ($p < 0.001$); Tukey HSD post-hoc tests confirmed Group IV > Group II, Group III, and Group I at $p < 0.001$ across all regenerative bone metrics (and lower Tb.Sp and residual CEJ–ABC vertical defect distance; $p < 0.001$).

Table 5. Balanced Two-Way Factorial ANOVA (Surgical Group × Healing Time, N = 40) and Week-8 Multi-Tissue Mechanistic Coupling Correlations (N = 20).

Analytical Model / Coupling Axis	Factor / Variable I	Factor / Variable II	Test Statistic (F / r)	Effect Magnitude (η_p² / R²)	p-value
Panel A: Two-Way Factorial ANOVA (N = 40)	Group Main Effect F(3,32)	Time Main Effect F(1,32)	Group × Time Interaction F(3,32)	Interaction η_p²	Interaction p-value
Alveolar Bone Volume Fraction (BV/TV)	297.81 (p < 0.001*)	301.28 (p < 0.001*)	F = 18.02	0.628	< 0.001*
Bone Mineral Density (BMD)	236.77 (p < 0.001*)	248.73 (p < 0.001*)	F = 8.41	0.441	0.0003*
Trabecular Thickness (Tb.Th)	185.97 (p < 0.001*)	178.21 (p < 0.001*)	F = 12.54	0.540	< 0.001*
Residual CEJ–ABC Crest Height	215.22 (p < 0.001*)	175.81 (p < 0.001*)	F = 4.75	0.308	0.0075*
CD31⁺ Microvessel Density	278.70 (p < 0.001*)	0.21 (p = 0.653)	F = 9.72	0.477	0.0001*
OCN⁺ Osteoblastic Matrix Area	257.89 (p < 0.001*)	130.72 (p < 0.001*)	F = 8.15	0.433	0.0004*
Panel B: Week-8 Mechanistic Coupling (N = 20)	Predictor Biological Axis	Target Structural Outcome	Pearson Correlation r	Variance Explained R²	Two-Tailed p-value
Angiogenic–Osteogenic Coupling	CD31⁺ Microvessel Density	Micro-CT Alveolar BV/TV (%)	r = 0.940	R² = 0.884	< 0.001*
Osteoblastic–Mineralization Axis	OCN⁺ Matrix Immunoreactivity	Micro-CT Alveolar BV/TV (%)	r = 0.970	R² = 0.941	< 0.001*
Matricellular–Fiber Guidance Axis	PDL Periostin (POSTN IOD)	Sharpey's Insertion Angle θ_PDL (°)	r = 0.932	R² = 0.869	< 0.001*
Matricellular–Cementogenic Axis	PDL Periostin (POSTN IOD)	New Cementum Thickness NCT (μm)	r = 0.971	R² = 0.943	< 0.001*

*Statistically significant at two-tailed $p < 0.05$. Group × Time interaction: group differences differed between Weeks 4 and 8. Additive contrast at Week 8 (Group IV − II − III + I, from the reported means and SDs with pooled error, 16 df): +5.8 percentage points BV/TV (95% CI −1.2 to 12.8; $p = 0.098$), versus +8.0 at Week 4 (95% CI 2.4 to 13.6; $p = 0.008$). Group IV exceeded the additive benchmark numerically at Week 8 (+54.0 vs. +48.2 percentage points expected from Group II [+29.4] + Group III [+18.8]). Panel B coefficients are pooled across the four groups (N = 20) and are descriptive.

Phase III: histomorphometry, Sharpey's fiber orientation, immunohistochemistry, and biosafety

Histological evaluation via H&E, Masson's trichrome, and polarized Picrosirius Red microscopy at Week 8 indicated that only Group IV showed new bone, a continuous neocementum layer and oriented fibers at Week 8 in this model, and no ankylosis or root resorption was observed in any group (0/5 roots across all groups; Figure 5A–C; Table 6). In Group I (OFD), defects collapsed inward and healed predominantly via long junctional epithelial downgrowth (JED = 1.62 ± 0.18 mm) and disorganized collagen fibers running nearly parallel to the denuded root dentin (θ_PDL = 14.8 ± 3.6°), with scant acellular cementum islands (NCT = 11.4 ± 2.4 μm; NBA = 20.8 ± 2.6%). Scaffoldless AGF-Gel (Group III) modestly enhanced basal bone islands (NBA = 38.4 ± 3.9%) and thin cementum (26.8 ± 3.8 μm) but failed to arrest apical epithelial migration (JED = 1.04 ± 0.14 mm) or

orient collagen insertion (θ_PDL = 24.6 ± 4.5°). Biphasic blank scaffolds (Group II) physically occluded epithelial downgrowth (JED = 0.58 ± 0.09 mm) and partially guided oblique fiber alignment via their 150-μm micro-channels (θ_PDL = 34.2 ± 4.1°).

In contrast, Group IV (3DBP–AGF) yielded 73.8 ± 3.7% new mature lamellar alveolar bone area ($F(3,16) = 204.68$, $p < 0.001$), a continuous 64.2 ± 4.8 μm neocementum layer lining the previously denuded root surface ($F(3,16) = 176.75$, $p < 0.001$), minimal epithelial downgrowth (0.21 ± 0.05 mm), and dense birefringent Type I/III Sharpey's collagen bundles inserting into both neocementum and bundle bone at a mean oblique angle of 50.8 ± 3.2°, close to the insertion angle of about 51° reported for the oblique fiber bundles of rat molar periodontium[50] (Figure 5A). Immunohistochemical staining indicated the following cellular associations: $CD31^+$ microvessel density peaked at Week 4 in Group IV (64.8 ± 4.4 vessels/mm² vs. 26.8 ± 3.1 in Group II and 42.6 ± 3.8 in Group III; $p < 0.001$) and remained high at Week 8 (58.2 ± 4.1 vessels/mm²), alongside OCN^+ osteoblastic matrix deposition (44.8 ± 3.1% at Week 8), 4.36 ± 0.31-fold normalized periostin (POSTN) expression across the regenerated PDL enthesis, and a high OPG/RANKL ratio of 3.28 ± 0.26 (vs. 0.74 ± 0.11 in OFD; $p < 0.001$).

Across the Week-8 cohort (N = 20, pooled across the four groups), $CD31^+$ microvascular density correlated strongly with Micro-CT BV/TV ($r = 0.940$, $p < 0.001$), while PDL POSTN expression correlated tightly with both Sharpey's fiber insertion angle ($r = 0.932$, $p < 0.001$) and neocementum thickness ($r = 0.971$, $p < 0.001$; Figure 5C; Table 5; correlations are pooled across the four groups and are therefore descriptive). Finally, somatic growth across time points (independent animals at each time point) (Week-8 weight 368.2–374.8 g; $p = 0.900$), hepatorenal serum biochemistry (ALT 39.8–42.2 U/L, $p = 0.865$; AST 83.6–87.2 U/L, $p = 0.872$; creatinine 0.52–0.55 mg/dL, $p = 0.844$), and systemic cytokines (TNF-α 18.9–21.4 pg/mL, $p = 0.480$; IL-10 32.6–38.4 pg/mL, $p = 0.158$) showed no difference among groups (n = 5 per group; the study was not designed to establish equivalence) (Figure 6A–B; Table 7).

Table 6. Phase III Periodontal Histomorphometry, Functional Sharpey's Fiber Angulation, and Immunohistochemical Coupling Across Surgical Groups.

Histomorphometric / IHC Endpoint	Group I: OFD Control (n = 5)	Group II: 3DBP- Blank (n = 5)	Group III: Autologous AGF-Gel (n = 5)	Group IV: Personalized 3DBP–AGF (n = 5)	ANOVA F(3,16) & Hedges' g (IV vs I)	p-value
$CD31^+$ Microvessel Density (vessels/mm²), Week 4	16.4 ± 2.4 [16.6; 16.5–16.8]	26.8 ± 3.1 [27.7; 25.3–28.5]	42.6 ± 3.8 [40.6; 40.1–43.3]	64.8 ± 4.4 [67.6; 61.2–67.9]	F = 180.45 (g_4v1 = 12.34)	< 0.001*
$CD31^+$ Microvessel Density (vessels/mm²), Week 8	19.2 ± 2.6 [19.1; 18.3–21.2]	34.4 ± 3.4 [36.0; 31.0–37.2]	36.8 ± 3.6 [35.7; 34.8–39.6]	58.2 ± 4.1 [59.2; 58.7–59.9]	F = 107.16 (g_4v1 = 10.26)	< 0.001*
Osteocalcin OCN^+ Matrix Area (%), Week 4	8.4 ± 1.3 [8.5; 8.1–8.8]	16.8 ± 1.9 [17.1; 17.0–17.2]	18.2 ± 2.1 [18.1; 16.6–19.7]	31.6 ± 2.6 [31.7; 31.5–32.8]	F = 111.86 (g_4v1 = 10.19)	< 0.001*
Osteocalcin OCN^+ Matrix Area (%), Week 8	12.6 ± 1.6 [12.5; 11.8–12.6]	26.4 ± 2.4 [27.5; 26.2–27.8]	23.8 ± 2.5 [23.4; 22.1–26.3]	44.8 ± 3.1 [44.6; 41.9–47.3]	F = 147.44 (g_4v1 = 11.79)	< 0.001*
New Alveolar Bone Area NBA (%), W8	20.8 ± 2.6 [21.0; 20.7–22.3]	48.6 ± 3.5 [49.6; 45.2–51.5]	38.4 ± 3.9 [38.7; 35.6–40.1]	73.8 ± 3.7 [71.6; 71.3–76.4]	F = 204.68 (g_4v1 = 14.97)	< 0.001*
New Cementum Thickness NCT (μm), W8	11.4 ± 2.4 [11.1; 9.5–13.8]	29.6 ± 3.6 [30.8; 29.2–31.9]	26.8 ± 3.8 [26.7; 24.3–26.8]	64.2 ± 4.8 [65.1; 62.9–66.1]	F = 176.75 (g_4v1 = 12.57)	< 0.001*
Sharpey's Fiber Angle θ_PDL (°), W8	14.8 ± 3.6 [15.2; 11.8–16.3]	34.2 ± 4.1 [33.5; 32.1–34.3]	24.6 ± 4.5 [25.0; 20.9–25.0]	50.8 ± 3.2 [51.3; 48.8–51.7]	F = 78.07 (g_4v1 = 9.55)	< 0.001*
Junctional Epithelial Downgrowth (mm), W8	1.62 ± 0.18 [1.53; 1.48–1.77]	0.58 ± 0.09 [0.59; 0.52–0.66]	1.04 ± 0.14 [1.04; 1.00–1.07]	0.21 ± 0.05 [0.19; 0.17–0.23]	F = 118.30 (g_4v1 = −9.64)	< 0.001*
Periostin POSTN Normalized IOD, W8	1.00 ± 0.14 [0.91; 0.91–1.04]	2.18 ± 0.22 [2.12; 2.11–2.15]	1.94 ± 0.24 [2.00; 1.99–2.08]	4.36 ± 0.31 [4.26; 4.24–4.30]	F = 182.17 (g_4v1 = 12.62)	< 0.001*

Histomorphometric / IHC Endpoint	Group I: OFD Control (n = 5)	Group II: 3DBP- Blank (n = 5)	Group III: Autologous AGF-Gel (n = 5)	Group IV: Personalized 3DBP–AGF (n = 5)	ANOVA F(3,16) & Hedges' g (IV vs I)	p-value
Anabolic OPG / RANKL Ratio, W8	0.74 ± 0.11 [0.71; 0.64–0.85]	1.68 ± 0.18 [1.65; 1.55–1.86]	1.52 ± 0.19 [1.60; 1.59–1.61]	3.28 ± 0.26 [3.20; 3.16–3.50]	F = 153.25 (g_4v1 = 11.49)	< 0.001*

Values expressed as mean ± SD [median; IQR]. Native uninjured rat mandibular molar Sharpey's fiber angle reference ≈ 51° (physiological oblique functional band 45°–60°). Zero dentoalveolar ankylosis or root resorption (0/5 roots) was observed across Groups I–IV. *Significant at two-tailed p < 0.001.

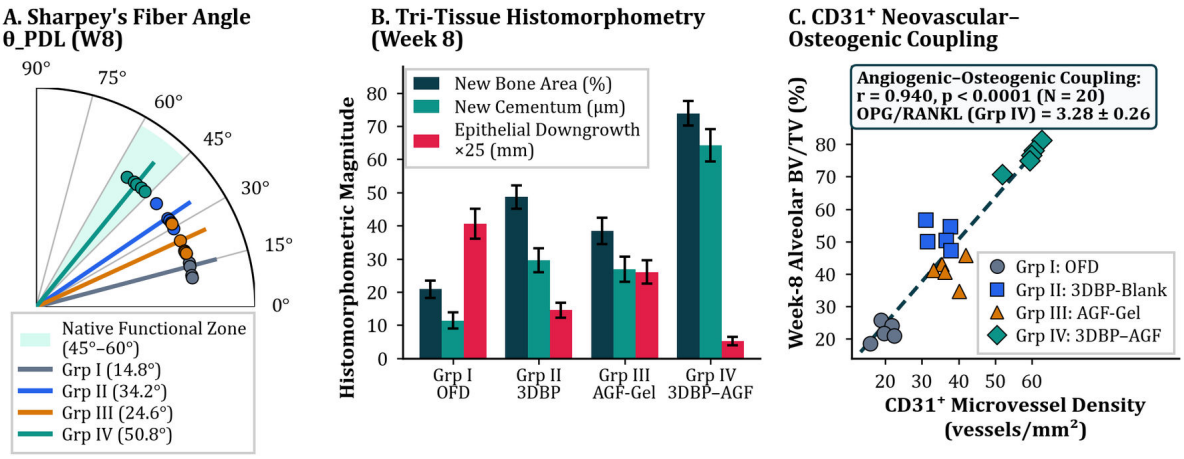

Figure 5. Phase III Week-8 periodontal histomorphometry, functional Sharpey's fiber insertion angulation, and immunohistochemical neovascular–osteogenic coupling (n = 5/group). (A) Polar angular distribution of regenerated Sharpey's collagen bundle insertion angles (θ_PDL) relative to the native physiological oblique zone (45°–60°). (B) New bone area (NBA, %), apical-notch-referenced new cementum thickness (NCT, μm), and suppression of pathological junctional epithelial downgrowth (JED, mm). (C) Linear regression coupling between CD31⁺ microvessel density and alveolar BV/TV across all Week-8 animals (N = 20).

Table 7. Phase III In Vivo Somatic Growth, Hepatorenal Biochemistry, and Systemic Inflammatory Cytokine Biosafety Profile at Week 8 (N = 20; n = 5/Group).

Systemic Biosafety Parameter	Group I: OFD Control (n = 5)	Group II: 3DBP- Blank (n = 5)	Group III: Autologous AGF-Gel (n = 5)	Group IV: Personalized 3DBP–AGF (n = 5)	One-Way ANOVA F(3,16) & η_p^2	p-value
Baseline Body Weight, Week 0 (g)	298.4 ± 11.2 [298.2; 296.2–306.6]	301.2 ± 10.8 [299.0; 296.5–301.4]	299.6 ± 11.5 [299.7; 290.4–304.4]	300.8 ± 10.6 [296.9; 293.2–307.5]	F = 0.07 (η_p^2 = 0.012)	0.977 (NS)
Terminal Body Weight, Week 8 (g)	368.2 ± 14.6 [365.7; 356.2–382.1]	372.4 ± 13.8 [370.8; 359.5–385.6]	370.6 ± 15.1 [371.8; 356.4–377.6]	374.8 ± 13.4 [373.9; 362.1–383.1]	F = 0.19 (η_p^2 = 0.035)	0.900 (NS)
Serum Alanine Aminotransferase ALT (U/L)	41.6 ± 4.8 [39.7; 37.8–46.2]	40.8 ± 4.5 [42.1; 40.1–43.1]	42.2 ± 5.1 [42.8; 38.3–43.8]	39.8 ± 4.4 [42.5; 37.1–42.6]	F = 0.24 (η_p^2 = 0.044)	0.865 (NS)
Serum Aspartate Aminotransferase AST (U/L)	86.4 ± 7.6 [87.3; 82.8–92.4]	84.8 ± 7.2 [86.0; 85.1–87.2]	87.2 ± 8.1 [88.4; 84.9–92.4]	83.6 ± 6.9 [81.6; 78.1–86.9]	F = 0.23 (η_p^2 = 0.042)	0.872 (NS)
Serum Creatinine (mg/dL)	0.54 ± 0.06 [0.53; 0.51–0.55]	0.53 ± 0.05 [0.53; 0.49–0.54]	0.55 ± 0.06 [0.57; 0.55–0.57]	0.52 ± 0.05 [0.54; 0.47–0.54]	F = 0.27 (η_p^2 = 0.049)	0.844 (NS)
Systemic Serum TNF-α (pg/mL)	21.4 ± 2.8 [22.4; 19.6–23.1]	20.6 ± 2.6 [20.9; 19.0–21.5]	19.8 ± 2.5 [18.5; 18.4–19.9]	18.9 ± 2.4 [18.8; 17.5–19.2]	F = 0.86 (η_p^2 = 0.139)	0.480 (NS)
Systemic Serum IL-10 (pg/mL)	32.6 ± 3.9 [31.5; 30.2–31.9]	34.2 ± 4.1 [33.6; 32.6–36.2]	36.8 ± 4.2 [36.2; 35.2–39.2]	38.4 ± 4.3 [37.7; 36.0–41.5]	F = 1.98 (η_p^2 = 0.270)	0.158 (NS)

NS: no statistically significant difference among groups (all p > 0.15). With n = 5 per group the data cannot exclude small differences, and no equivalence test was performed.

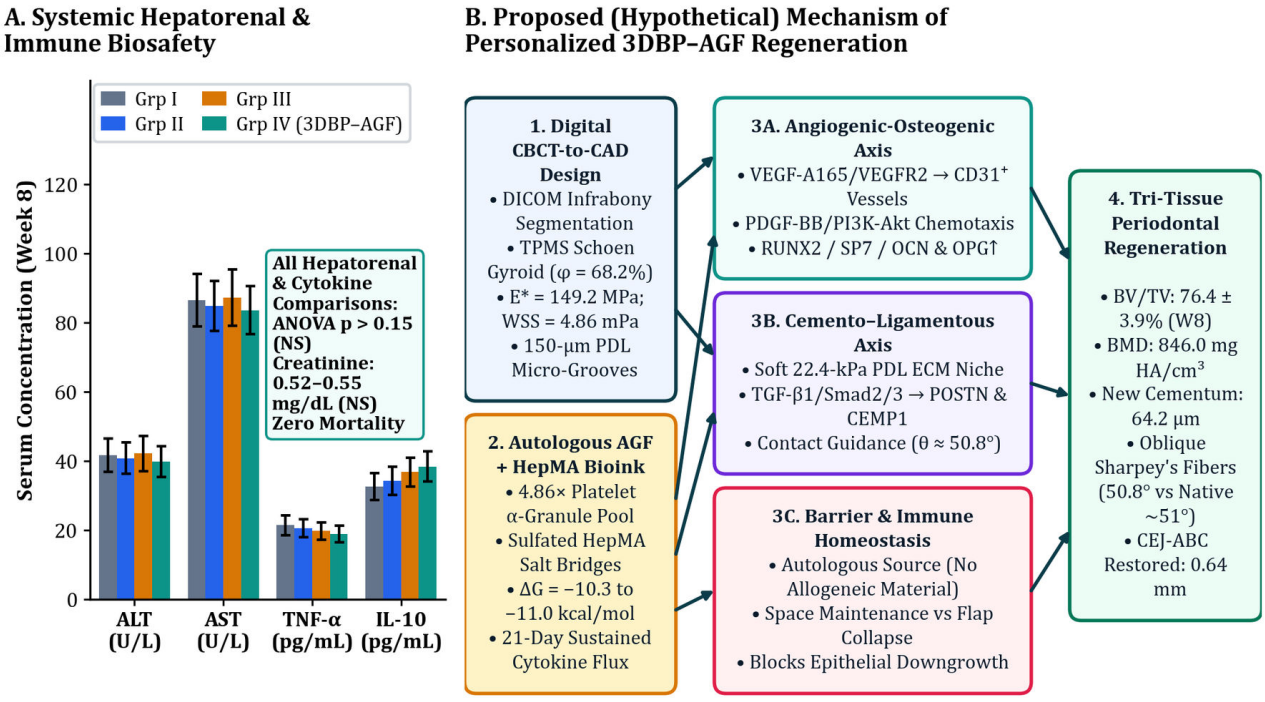

Figure 6. Systemic in vivo biosafety profile and integrative translational mechanism. (A) Week-8 serum hepatorenal transaminases (ALT, AST) and systemic pro-/anti-inflammatory cytokines (TNF-α, IL-10) showing no detectable difference among Groups I–IV (all ANOVA p > 0.15; n = 5 per group). (B) Proposed (hypothetical) mechanism by which CBCT-guided biphasic TPMS GelMA–HepMA/nHAp 3D bioprinting and sequestered autologous AGF may coordinate angiogenesis, osteogenesis, and oblique Sharpey's fiber insertion.

4. Discussion

Principal findings

Reconstructing complex Stage III and Stage IV periodontal alveolar defects remains one of the most challenging problems in regenerative dental medicine. Therapy requires synchronous restoration of vascularized cancellous-cortical bone, root-investing cementum, and a biomechanically functional, unmineralized periodontal ligament across a contaminated, masticatory-loaded dentoalveolar interface.[4–8] In the present tri-modal translational investigation, we combined computational scaffold topology and affinity-hydrogel modeling (Phase I), controlled bioink printability and primary human stem cell differentiation assays (Phase II), and critical-size rat mandibular defect reconstruction (Phase III), with the aim of testing whether integrating CBCT-guided biphasic 3D bioprinting with autologous Activated Growth Factor (AGF) overcomes the two clinical failure modes of conventional bone substitutes and soluble autologous platelet concentrates. In this model, neither structural 3D printing alone (Group II: Week-8 BV/TV 51.8 ± 3.8%) nor unencapsulated autologous AGF gel alone (Group III: 41.2 ± 4.1%) was sufficient to regenerate a complete periodontal attachment apparatus.

Integrating autologous AGF within a sulfated HepMA-functionalized, biphasic TPMS Schoen Gyroid GelMA/nHAp construct (Group IV) was associated with a significant Group × Time interaction ($F = 18.02$, $p < 0.001$), indicating that group differences widened between Week 4 and Week 8. By Week 8, this construct restored 76.4 ± 3.9% alveolar bone volume fraction, 64.2 ± 4.8 μm neocementum, and 50.8 ± 3.2° oblique Sharpey's fiber insertion. These quantitative

computational, cellular, and preclinical animal findings advance our previously published conceptual hypothesis.[7] They suggest that structural additive manufacturing and autologous secretome pharmacology act as complementary partners. The 3D-bioprinted lattice may prevent soft-tissue collapse of the biologic reservoir. Affinity-bound AGF may turn a passive osteoconductive framework into a chemotactically active, self-vascularizing regenerative niche.

Scaffold architecture and in silico mechanobiology

From a biomechanical and dental engineering standpoint, our Phase I computational analyses suggest that internal pore geometry and anatomical personalization influence early wound stability in non-contained periodontal defects. Clinical cohort studies of patient-specific 3D-printed scaffolds report that inaccurate marginal adaptation creates dead space, promotes mucosal dehiscence, and concentrates occlusal shear along thin buccal cortical plates.[10,11] Our fabrication workflow coupled sub-100-μm CBCT segmentation with photo-crosslinkable shear-thinning GelMA–HepMA/nHAp bioinks (CAD-to-print surface RMSD 72.5 ± 5.8 μm; Pr = 0.99 ± 0.02). This achieved press-fit defect adaptation. Simulated masticatory micromotion under a 150-N oblique molar load was computed as 12.63 μm, below the 28-μm level up to which bone ingrowth into porous implants has been observed, whereas micromotion of 150 μm or more led to fibrous tissue attachment.[51,5217,19] Replacing conventional 0°/90° rectilinear struts with an implicit TPMS Schoen Gyroid surface eliminated orthogonal stress-riser junctions and reduced peak Von Mises stress from 18.60 MPa to 8.78 MPa, while the same change raised Darcy permeability 2.62-fold to 6.40 × 10^{-9} m^2.[17–20] This agrees with recent mechanobiology studies of TPMS bone repair.[17,18] In the simulation, continuous gyroid helicoidal channels converted physiological interstitial fluid movement into a narrow wall shear stress regime considered osteoinductive (4.86 ± 0.89 mPa across 91.6% of internal pore area). This regime is proposed to activate mechanosensitive piezo1/integrin–FAK–YAP/TAZ signaling (not measured here) in colonizing osteoprogenitors even prior to full vascular maturation.

Biphasic interface and prevention of ankylosis

The monolithic biphasic stiffness and topographical architecture engineered into the root-scaffold interface may be equally relevant to preventing dentoalveolar ankylosis. Historical attempts to pack stiff ceramic granules or rigid thermoplastic scaffolds directly against curetted root dentin frequently induced localized root resorption or bony fusion, because rigid substrates (>100 kPa) drive osteogenic mechanotransduction at the expense of ligamentous homeostasis.[9,11,25] Our construct juxtaposed a nanohydroxyapatite-reinforced gyroid alveolar compartment (measured hydrated-construct compressive modulus 182.6 ± 12.1 kPa; simulated solid strut composite modulus 149.16 MPa, which refers to a different material scale) against a nanoparticle-free, 150-μm micro-grooved GelMA–HepMA periodontal compartment tuned to 22.4 ± 1.6 kPa, and in this way it recapitulated the native mechanobiological boundary separating mineralized bundle bone from unmineralized PDL matrix.[8,15,25] In vivo polarized Picrosirius Red histomorphometry was consistent with a functional benefit of this two-zone design. Even without exogenous biologics, the micro-grooved 3DBP-Blank scaffold (Group II) shifted collagen insertion angles from pathological parallel alignment in OFD controls (14.8 ± 3.6°) to 34.2 ± 4.1° and curtailed epithelial downgrowth by 64.2% (0.58 ± 0.09 mm vs. 1.62 ± 0.18 mm).

It acted as an intrinsic barrier. This resorbable spatial barrier may reduce the need for a separate non-resorbable GTR membrane.[8,10,15] Mechanistically, this ~8.2-fold local hydrogel modulus step-down between the nHAp-reinforced osteogenic zone (182.6 ± 12.1 kPa) and the ceramic-free micro-grooved PDL interface (22.4 ± 1.6 kPa) is proposed to provide spatially segregated mechanotransductive instruction across the regenerating enthesis.[25,42,45] Within the stiffer, calcium-phosphate-rich alveolar lattice, high

cytoskeletal actomyosin tension may promote nuclear translocation of the mechanosensors YAP and TAZ. These may co-activate RUNX2 and SP7 transcription and thereby support lamellar bone mineralization.[25,42,53] Within the compliant 22.4-kPa root-facing micro-channels, by contrast, attenuated substrate stiffness may restrain ectopic osteogenic mineralization. At the same time, aligned topographical strain and TGF-β1 signaling may upregulate the tendon/ligament homeobox factor Mohawk (Mkx), periostin (POSTN), and cementum protein-1 (CEMP1).[44,45,47] This may help explain why Group IV specimens showed a mean neocementum thickness of 64.2 ± 4.8 μm and a mean oblique Sharpey's fiber angle of 50.8 ± 3.2°, with no dentoalveolar ankylosis.

Growth factor affinity, release, and platelet concentrates

In terms of biological agent pharmacology, the Phase I docking calculations and Phase II release kinetics reported here address a longstanding paradox in clinical platelet concentrate therapy. Network meta-analyses and systematic reviews confirm that autologous PRP, PRF, and activated growth factor preparations improve probing depth reduction and clinical attachment gain in contained three-wall intrabony defects.[29–31,34] Their efficacy in wide or non-contained alveolar defects, however, remains erratic.[30,35] Two mechanisms may explain this clinical ceiling. Mechanically, native fibrin clots have low compressive resistance (<5 kPa) and collapse beneath mucoperiosteal flaps, and our Group III (AGF-Gel) animals mirrored this directly: early Week-4 bone formation (26.8 ± 3.1%) stagnated at Week 8 (41.2 ± 4.1%), alongside persistent residual crestal loss (1.68 ± 0.14 mm). Pharmacologically, passive bolus adsorption onto standard hydrogels (G2) led to 72.6%–79.4% burst release of TGF-β1, VEGF-A165, and PDGF-BB within 24 hours.[28,32] Covalent grafting of 1.5% (w/v) sulfated HepMA is predicted to turn the GelMA hydrogel into an affinity reservoir. It is predicted to engage conserved cationic Arg/Lys clusters on PDGF-BB (Arg27/Arg28/Lys80/Lys81; K_d = 18.93 nM), VEGF-A165 (Arg123/Arg124/Lys140/Arg145; K_d = 29.81 nM), and TGF-β1 (Arg25/Lys31/Arg94; K_d = 53.46 nM), with >5,000-fold stronger affinity than unmodified GelMA, while the receptor-binding interfaces remained sterically unhindered in the docked poses (RMSD < 0.72 Å).[28,36,37]

As a result, the 24-hour PDGF-BB burst loss fell fourfold to 19.8 ± 2.1%, which, together with the 21-day release profile, is consistent with a sustained cytokine supply during collagenase-mediated hydrogel remodeling (64.2 ± 3.1% Day-28 retention). Sulfated HepMA conjugation may also confer biochemical protection within proteolytically hostile periodontal wounds, beyond slowing passive diffusive escape. Inflamed gingival crevicular exudates contain abundant serine proteases, plasmin, and matrix metalloproteinases, which cleave unbound PDGF-BB and VEGF-A165 within hours in vivo.[28,37] By mimicking native heparan sulfate proteoglycans, bidentate sulfate-to-arginine salt bridges may sterically shield basic proteolytic cleavage loops and stabilize the tertiary homodimeric conformation of sequestered AGF cytokines, while our leukocyte-poor centrifugation and 0.22-μm filtration protocol, in turn, is expected to have limited co-encapsulation of neutrophil MMP-8/MMP-9 and catabolic Wnt inhibitors, so that both the GelMA hydrogel architecture and sustained morphogen bioactivity may have been preserved throughout the 21-day Korsmeyer–Peppas release window (n_KP = 0.45–0.47; proteolytic protection and MMP content were not measured).[28,29,32]

Cellular and molecular signaling (proposed mechanisms)

At the cellular and molecular signaling level, sustained co-delivery of autologous AGF morphogens was associated with coordinated angiogenic, osteogenic, and cementogenic responses.[7,42,46] In the acute healing window (Days 1–14), sequestered VEGF-A165 and PDGF-BB stimulated HUVEC capillary network assembly in vitro (12.14 ± 0.84 mm/field). They were also associated with a 3.95-fold increase in

Week-4 $CD31^+$ microvessel density in vivo (64.8 ± 4.4 vs. 16.4 ± 2.4 vessels/mm^2 in OFD). CD31-high neovessels may resemble mechanosensitive Type H capillaries (identification requires CD31 and endomucin staining, not performed here), which have been implicated in occlusal alveolar bone homeostasis,[46,48] and these vessels may have prevented central scaffold hypoxia and secreted paracrine osteogenic angiokines that, together with silicate-nHAp $Ca^{2+}/PO_4^{3-}/SiO_4^{4-}$ ion dissolution,[25–27,41] may have activated the PI3K/Akt–RUNX2–SP7 transcriptional cascade in resident and recruited hPDLSCs (RUNX2 4.26-fold; BGLAP 4.88-fold; Week-8 CD31 vs. BV/TV $r = 0.940$, $p < 0.001$). Within the softer 22.4-kPa root-interfacing micro-channels, sustained TGF-β1/Smad2/3 signaling and topographical contact guidance may have upregulated cementum protein-1 (CEMP1, 3.76-fold). Periostin (POSTN) rose 4.18-fold in vitro and 4.36-fold IOD in vivo.[44,45]

Periostin and Mohawk-regulated matricellular assembly are considered important for cross-linking collagen fibrillogenesis across the PDL–cementum enthesis and for suppressing aberrant mineralization within the ligament space.[45,47] The tight linear coupling observed between POSTN expression, 64.2-μm neocementum deposition ($r = 0.971$), and physiological 50.8° oblique Sharpey's fiber insertion ($r = 0.932$) is compatible with this role. Elevated OPG/RANKL ratios (3.28 ± 0.26) may also have restrained osteoclastic crestal resorption.[33,43] A late remodeling transition followed between Week 4 and Week 8. Cell-mediated enzymatic degradation gradually resorbed the GelMA–HepMA hydrogel network (64.2% mass retention at Day 28), while progressive dissolution of bioactive Ca^{2+}, PO_4^{3-}, and orthosilicate ions from the 5% (w/v) silicate-substituted nHAp phase supplied sustained inorganic mineral building blocks and osteoconductive nucleation sites that may have acted together with early AGF-associated $CD31^+$ microvascular beds to mature woven osteoid into dense 846.0 mg HA/cm^3 alveolar bone.[25–27,46] None of these pathways (piezo1/YAP-TAZ, PI3K/Akt, Smad2/3, Mkx) or the identity of Type H vessels was measured in this study; the mechanisms described here are hypotheses.

Strengths, limitations, and translational workflow

This study has several methodological strengths and translational limitations. Its primary strength is end-to-end internal consistency, since parameters derived ab initio in Phase I (TPMS Gyroid porosity/stiffness and HepMA–cytokine dissociation constants) informed the Phase II formulation; the Phase II release data are consistent with sustained release, while the four-arm preclinical factorial design cleanly separated scaffold structural conduction (Group II) and soluble autologous growth factor bioactivity (Group III) from the combined bio-integrated effect (Group IV). Reliance on leukocyte-modulated autologous AGF alone circumvented allogeneic immunogenicity. It was also not associated with detectable systemic hepatorenal or pro-inflammatory toxicity (serum ALT, AST, creatinine, and TNF-α all $p > 0.45$ at Week 8). Acute surgically created mandibular defects in young adult rats heal faster than human defects. They lack the chronic polymicrobial dysbiosis, lipopolysaccharide-primed M1 macrophage polarization, and compromised vascularity characteristic of longstanding human Stage III–IV periodontitis pockets or diabetic hosts.[4,36,47] Further limitations include the use of male rats only; $n = 5$ per group and only two time points (Weeks 4 and 8); the absence of an uninjured control group; the absence of in vivo mechanical and degradation testing; simulated values obtained from MM-GBSA and a single scaffold geometry; and primary cells from a limited number of donors.

Chairside translation of personalized CBCT-to-bioprinter workflows will also require Good Manufacturing Practice (GMP)-compliant closed-cartridge bioink sterilization, standardized point-of-care platelet activation kits to minimize inter-patient donor variability in baseline α-granule cytokine titers,[32] and it will also require validation in chronically infected large-animal (canine or miniature

swine) class III furcation and one-wall infrabony models before first-in-human randomized clinical trials. The modular design developed here is projected to be compatible with single-visit chairside periodontal surgery. Diagnostic CBCT segmentation and biphasic TPMS G-code generation are projected to be completed preoperatively within about 15 minutes. The AGF protocol described in the Methods requires about 65 minutes of centrifugation and activation, so venipuncture and AGF preparation would have to start before, or run in parallel with, flap elevation and root debridement. Sterile cartridge mixing with pre-lyophilized GMP GelMA–HepMA/nHAp, followed by rapid 405-nm visible-light bioprinting (<10 minutes per defect-specific graft), allows chairside press-fit implantation. Whether the whole workflow fits within a standard 60-to-75-minute regenerative periodontal appointment depends on that parallel preparation and has not been tested.[10–12]

5. Conclusion

Combining CBCT-guided biphasic TPMS Schoen Gyroid 3D bioprinting (GelMA–HepMA/nHAp) with standardized Autologous Activated Growth Factor (AGF) gave preclinical support for a personalized periodontal regeneration platform. In a rat defect model, the combination regenerated alveolar bone, cementum, and an oriented periodontal ligament. Simulation predicted cancellous-matched stability and uniform osteogenic perfusion shear stress for the gyroid lattice. The soft, 150-μm micro-grooved periodontal interface accompanied oblique collagen alignment and no ankylosis. Sulfated HepMA, predicted to bind growth factors electrostatically, cut 24-hour PDGF-BB burst release from 79.4 ± 4.2% to 19.8 ± 2.1%. Over 21 days, sustained delivery of PDGF-BB, VEGF-A165, and TGF-β1 was associated with $CD31^+$ neovascularization, RUNX2/SP7/OCN-associated bone regeneration (76.4 ± 3.9% BV/TV at Week 8), neocementum, and Sharpey's fiber insertion. No systemic toxicity was detected. These findings support further preclinical evaluation of chairside affinity-bioprinted autologous biologics.

Declarations

Ethics approval and consent to participate

All animal procedures and the primary human cell protocols were reviewed and approved by the Ethics Committee of CMHC Research Center (Protocol Number: 331/2025) and were conducted in accordance with the ARRIVE 2.0 guidelines and, for human material, the Declaration of Helsinki.

Consent for publication

Not applicable.

Funding

The authors received no funding for this study.

Competing interests

The authors declare no commercial, financial, or personal conflicts of interest related to the biomaterials, computational workflows, or biological protocols investigated in this study.

Author contributions

Z.D.: conceptualization, investigation (CBCT-to-CAD scaffold modeling, in vitro and in vivo experiments), data curation, writing – original draft. R.H.: conceptualization, methodology (study methodology and standardization of the autologous biological agent), formal analysis (biostatistical supervision), supervision, project administration, writing – review & editing. M.A.: software and formal analysis (molecular docking and finite element simulation), investigation (histomorphometric quantification), visualization, writing – review & editing. All authors read and approved the final manuscript.

Data availability

All data are available from corresponding author on reasonable academic request.

Generative AI disclosure

No generative AI tools were used in the preparation of this manuscript.

Acknowledgments

The authors have no acknowledgments to declare.

6. References

1. Nascimento GG, Alves-Costa S, Romandini M. Burden of severe periodontitis and edentulism in 2021, with projections up to 2050: The Global Burden of Disease 2021 study. J Periodontal Res. 2024;59(5):823-867. doi:10.1111/jre.13337
2. Chen MX, Zhong YJ, Dong QQ, Wong HM, Wen YF. Global, regional, and national burden of severe periodontitis, 1990–2019: An analysis of the Global Burden of Disease Study 2019. J Clin Periodontol. 2021;48(9):1165-1188. doi:10.1111/jcpe.13506
3. Dai X, Tao Y, Zhou J, Zhou Y, Liang S, Ma X. Global burden and trends of severe periodontitis among women of childbearing age, 1990–2021. J Periodontol. 2025:JPER.24-0615. doi:10.1002/jper.24-0615
4. Papapanou PN, Sanz M, Buduneli N, Dietrich T, Feres M, Fine DH, et al. Periodontitis: Consensus report of workgroup 2 of the 2017 World Workshop on the Classification of Periodontal and Peri-Implant Diseases and Conditions. J Clin Periodontol. 2018;45(S20):S162-S170. doi:10.1111/jcpe.12946
5. Sanz M, Herrera D, Kebschull M, Chapple I, Jepsen S, Berglundh T, et al. Treatment of stage I–III periodontitis—The EFP S3 level clinical practice guideline. J Clin Periodontol. 2020;47(S22):4-60. doi:10.1111/jcpe.13290
6. Herrera D, Sanz M, Kebschull M, Jepsen S, Sculean A, Berglundh T, et al. Treatment of stage IV periodontitis: The EFP S3 level clinical practice guideline. J Clin Periodontol. 2022;49(S24):4-71. doi:10.1111/jcpe.13639
7. Dapala Z, Hidayat R, Ashraf M. Personalized Periodontal Regeneration: Integrating 3D Bioprinting with Autologous Activated Growth Factor (AGF) for Enhanced Alveolar Bone Defect Healing. Biosci Med. 2025;9(12):9995-10007. doi:10.37275/bsm.v9i12.1605
8. Sufaru IG, Macovei G, Stoleriu S, Martu MA, Luchian I, Kappenberg-Nitescu DC, et al. 3D printed and bioprinted membranes and scaffolds for the periodontal tissue regeneration: A narrative review. Membranes (Basel). 2022;12(9):902. doi:10.3390/membranes12090902
9. Goldberg M. The Periodontal Ligament-A Link between the Cementum and Alveolar Bone. J Clin Med Res. 2022;03(01). doi:10.46889/jcmr.2022.3106
10. Verykokou S, Ioannidis C, Angelopoulos C. CBCT-Based Design of Patient-Specific 3D Bone Grafts for Periodontal Regeneration. J Clin Med. 2023;12(15):5023. doi:10.3390/jcm12155023
11. Ivanovski S, Staples R, Arora H, Vaquette C, Alayan J. Alveolar bone regeneration using a 3D-printed patient-specific resorbable scaffold for dental implant placement: A case report. Clin Oral Implants Res. 2024;35(12):1655-1668. doi:10.1111/clr.14340
12. Das S, Valoor R, Jegadeesan JT, Basu B. 3D bioprinted GelMA scaffolds for clinical applications: Promise and challenges. Bioprinting. 2024;44:e00365. doi:10.1016/j.bprint.2024.e00365
13. Shahrezaie M, Zamanian A, Sahranavard M, Shahrezaee MH. A critical review on the 3D bioprinting in large bone defects regeneration. Bioprinting. 2024;37:e00327. doi:10.1016/j.bprint.2023.e00327
14. Codrea CI, Baykara D, Mitran RA, Koyuncu ACC, Gunduz O, Ficai A. 3D-bioprinted gelatin methacryloyl-strontium-doped hydroxyapatite composite hydrogels scaffolds for bone tissue regeneration. Polymers. 2024;16(13):1932. doi:10.3390/polym16131932
15. Sowmya S, Mony U, Jayachandran P, Reshma S, Kumar RA, Arzate H, et al. Tri-layered nanocomposite hydrogel scaffold for the concurrent regeneration of cementum, periodontal ligament, and alveolar bone. Adv Healthc Mater. 2017;6(7):1601251. doi:10.1002/adhm.201601251
16. Kim JI, Kim JY, Bhattarai G, So HS, Kook SH, Lee JC. Periodontal ligament-mimetic fibrous

scaffolds regulate YAP-associated fibroblast behaviors and promote regeneration of periodontal defect in relation to the scaffold topography. ACS Appl Mater Interfaces. 2022;15(1):599-616. doi:10.1021/acsami.2c18893

17. Hayashi K, Kishida R, Tsuchiya A, Ishikawa K. Superiority of triply periodic minimal surface gyroid structure to strut-based grid structure in both strength and bone regeneration. ACS Appl Mater Interfaces. 2023;15(29):34570-34577. doi:10.1021/acsami.3c06263
18. Liu S, Feng J, Zhang F, Jiang W, Vasilieva TM, Lu P, et al. Parametric design and performance study of continuous gradient triply periodic minimal surface bone scaffold. Int J Bioprint. 2024;10(2):2306. doi:10.36922/ijb.2306
19. Araya M, Murillo J, Vindas R, Guillén T. Compressive behavior of SLA open-cell lattices: A comparison between triply periodic minimal surface gyroid and stochastic structures for artificial bone. Materialia. 2024;38:102233. doi:10.1016/j.mtla.2024.102233
20. Gabrieli R, Schiavi A, Pennecchi FR, Alidoost D, Schwentenwein M, D'Andrea L, et al. Permeability and microstructural parameters of 3D-printed triply periodic minimal surface (TPMS) hydroxyapatite scaffolds. J Am Ceram Soc. 2025;108(11):e70104. doi:10.1111/jace.70104
21. Wang N, Meenashisundaram GK, Kandilya D, Fuh JYH, Dheen ST, Kumar AS. A biomechanical evaluation on Cubic, Octet, and TPMS gyroid Ti6Al4V lattice structures fabricated by selective laser melting and the effects of their debris on human osteoblast-like cells. Biomater Adv. 2022;137:212829. doi:10.1016/j.bioadv.2022.212829
22. Iervolino F, Belgio B, Bonessa A, Potere F, Suriano R, Boschetti F, et al. Versatile and non-cytotoxic GelMA-xanthan gum biomaterial ink for extrusion-based 3D bioprinting. Bioprinting. 2023;31:e00269. doi:10.1016/j.bprint.2023.e00269
23. Jongprasitkul H, Turunen S, Parihar VS, Kellomäki M. Sequential Cross-linking of Gallic Acid-Functionalized GelMA-Based Bioinks with Enhanced Printability for Extrusion-Based 3D Bioprinting. Biomacromolecules. 2023;24(1):502-514. doi:10.1021/acs.biomac.2c01418
24. Su JJM, Lin CH, Chen H, Lee SY, Lin YM. Biofabrication of cell-laden gelatin methacryloyl hydrogels with incorporation of silanized hydroxyapatite by visible light projection. Polymers. 2021;13(14):2354. doi:10.3390/polym13142354
25. Das S, Basu B. Extrusion-based 3D printing of gelatin methacryloyl with nanocrystalline hydroxyapatite. Int J Appl Ceram Technol. 2021;19(2):924-938. doi:10.1111/ijac.13885
26. Allen NB, Abar B, Johnson L, Burbano J, Danilkowicz RM, Adams SB. 3D-bioprinted GelMA-gelatin-hydroxyapatite osteoblast-laden composite hydrogels for bone tissue engineering. Bioprinting. 2022;26:e00196. doi:10.1016/j.bprint.2022.e00196
27. Wang W, Zhu Y, Liu Y, Chen B, Li M, Yuan C, et al. 3D bioprinting of DPSCs with GelMA hydrogel of various concentrations for bone regeneration. Tissue Cell. 2024;88:102418. doi:10.1016/j.tice.2024.102418
28. Wang J, Xiao L, Wang W, Zhang D, Ma Y, Zhang Y, et al. The Auxiliary Role of Heparin in Bone Regeneration and its Application in Bone Substitute Materials. Front Bioeng Biotechnol. 2022;10:837172. doi:10.3389/fbioe.2022.837172
29. Cui Y, Mai Y, Liu X, Mu H. Clinical benefits of autologous platelet concentrate in periodontal intrabony defects: A network meta-analysis of randomized controlled trials. Eur J Oral Sci. 2024;132(3):e12978. doi:10.1111/eos.12978
30. Varshney S, Dwivedi A, Dwivedi V. Comparing efficacies of autologous platelet concentrate

preparations as mono-therapeutic agents in intra-bony defects through systematic review and meta-analysis. J Oral Biol Craniofac Res. 2023;13(6):671-681. doi:10.1016/j.jobcr.2023.08.007

31. Anitua E, Allende M, Alkhraisat M. Unravelling Alveolar Bone Regeneration Ability of Platelet-Rich Plasma: A Systematic Review with Meta-Analysis. Bioengineering. 2022;9(10):506. doi:10.3390/bioengineering9100506
32. Husak V, Povelychenko O, Maltseva V, Romanenko K, Vorontsov P, Pazdnikov R. Growth factor and cell content in Platelet-Rich Plasma (PRP), Leukocyte- and Platelet-Rich Plasma (L-PRP), Platelet-Rich Fibrin (PRF) in patients with long bone defects from combat injuries. BMC Musculoskelet Disord. 2025;26(1):1106. doi:10.1186/s12891-025-09346-9
33. Srinivas S, Sethuraman S, Krishnavilasom Jayakumari N. Evaluation of Osteocalcin Level in Gingival Crevicular Fluid in Periodontal Intrabony Defects Treated with Autologous Platelet Rich Fibrin: Non-Randomized Experimental Study. J Oral Maxillofac Res. 2024;15(4). doi:10.5037/jomr.2024.15403
34. Ye L, Mashrah MA, Ge L, Fang Y, Guo X, Ge Q, et al. Network meta-analysis of platelet-rich fibrin in periodontal intrabony defects. J Oral Pathol Med. 2023;52(3):206-215. doi:10.1111/jop.13409
35. Miron RJ, Moraschini V, Estrin N, Shibli JA, Cosgarea R, Jepsen K, et al. Autogenous platelet concentrates for treatment of intrabony defects-A systematic review with meta-analysis. Periodontol 2000. 2024;97(1):153-190. doi:10.1111/prd.12598
36. Li Y, Liu Z, Zhao C, Xu C, Shin A, Wu J, et al. A sustained-release PDGF-BB nanocomposite hydrogel for DM-associated bone regeneration. J Mater Chem B. 2023;11(5):974-984. doi:10.1039/d2tb02037h
37. Wang JF, Jan JS, Hu JJ. Heparin-Based Growth Factor Delivery Platforms: A Review. Pharmaceutics. 2025;17(9):1145. doi:10.3390/pharmaceutics17091145
38. Yuan Y, Zhao X, Hu J, Zhu Y, Deng X, Jiang Q. Bilayer oxidized sodium alginate–carboxymethyl chitosan hydrogel microspheres enable sustained BMP-2 release for enhanced bone regeneration. Biomed Mater. 2025;20(6):065009. doi:10.1088/1748-605x/ae0778
39. Claaßen C, Sewald L, Tovar G, Borchers K. Controlled Release of Vascular Endothelial Growth Factor from Heparin-Functionalized Gelatin Type A and Albumin Hydrogels. Gels. 2017;3(4):35. doi:10.3390/gels3040035
40. Percie du Sert N, Hurst V, Ahluwalia A, Alam S, Avey MT, Baker M, et al. The ARRIVE guidelines 2.0: Updated guidelines for reporting animal research. BMC Vet Res. 2020;16(1):242. doi:10.1186/s12917-020-02451-y
41. Zhao Q, Li G, Wang T, Jin Y, Lu W, Ji J. Human Periodontal Ligament Stem Cells Transplanted with Nanohydroxyapatite/Chitosan/Gelatin 3D Porous Scaffolds Promote Jaw Bone Regeneration in Swine. Stem Cells Dev. 2021;30(10):548-559. doi:10.1089/scd.2020.0204
42. Ru L, Pan B, Zheng J. Signalling pathways in the osteogenic differentiation of periodontal ligament stem cells. Open Life Sci. 2023;18(1):20220706. doi:10.1515/biol-2022-0706
43. Shao X, Wu F, Song Y, Kong R, Wang S, Wang L. The Effects of Different Developmental Stages on Bone Regeneration of Periodontal Ligament Stem Cells and Periodontal Ligament Cell Sheets In Vitro and Vivo. Stem Cells Dev. 2024;33(21-22):595-606. doi:10.1089/scd.2024.0087
44. Hoz L, López S, Zeichner-David M, Arzate H. Regeneration of rat periodontium by cementum protein 1-derived peptide. J Periodontal Res. 2021;56(6):1223-1232. doi:10.1111/jre.12921
45. Yagasaki L, Chiba T, Kurimoto R, Nakajima M, Iwata T, Asahara H. The essential role of Mkx in periodontal ligament on the metabolism of alveolar bone and cementum. Regen Ther.

2024;25:186-193. doi:10.1016/j.reth.2023.12.007

46. Li S, Cai X, Guo J, Li X, Li W, Liu Y, et al. Cell communication and relevant signaling pathways in osteogenesis–angiogenesis coupling. Bone Res. 2025;13(1):45. doi:10.1038/s41413-025-00417-0
47. Sone ED, McCulloch CA. Periodontal regeneration: Lessons from the periodontal ligament-cementum junction in diverse animal models. Front Dent Med. 2023;4:1124968. doi:10.3389/fdmed.2023.1124968
48. Chen Y. Occlusal Force Maintains Alveolar Bone Homeostasis Via Type H Angiogenesis. Int Dent J. 2025;75:104423. doi:10.1016/j.identj.2025.104423
49. Sun J, Wang H, Xiao J, Yang Q, Liu H, Yang Z, et al. Chamomile tincture and lidocaine hydrochloride gel ameliorates periodontitis: a preclinical study. Biomedicines. 2024;12(11):2629. doi:10.3390/biomedicines12112629
50. Liang Y, Hu Z, Chang B, Liu X. Quantitative characterizations of the Sharpey's fibers of rat molars. J Periodontal Res. 2020;55(2):307-314. doi:10.1111/jre.12716
51. Pilliar RM, Lee JM, Maniatopoulos C. Observations on the effect of movement on bone ingrowth into porous-surfaced implants. Clin Orthop Relat Res. 1986;(208):108-113. doi:10.1097/00003086-198607000-00023
52. Jasty M, Bragdon C, Burke D, O'Connor D, Lowenstein J, Harris WH. In vivo skeletal responses to porous-surfaced implants subjected to small induced motions. J Bone Joint Surg Am. 1997;79(5):707-714. doi:10.2106/00004623-199705000-00010
53. Shi Z, Zhong Q, Chen Y, Gao J, Pan X, Lian Q, et al. Nanohydroxyapatite, Nanosilicate-Reinforced Injectable, and Biomimetic Gelatin-Methacryloyl Hydrogel for Bone Tissue Engineering. Int J Nanomedicine. 2021;16:5603-5619. doi:10.2147/ijn.s321387